

## Guangqi: A two-dimensional radiation hydrodynamic code with realistic equation of states

ZHUO CHEN(陈卓)  <sup>1</sup> AND XUE-NING BAI (白雪宁)  <sup>1,2</sup>

<sup>1</sup> *Institute for Advanced Study, Tsinghua University  
 Beijing 100084, China*

<sup>2</sup> *Department of Astronomy, Tsinghua University  
 Beijing 100084, China*

Submitted to ApJS

### ABSTRACT

We present **Guangqi**, a new two-dimensional, finite-volume radiation hydrodynamics code designed for high-performance astrophysical simulations. The code simultaneously resolves the hydrodynamic equations for complex equations of state (EoS) and implicit radiation transport under the flux-limited diffusion approximation. Written in Fortran and parallelized via the Message Passing Interface. **Guangqi** supports analytic hydrogen and helium EoS under the assumption of local thermal and chemical equilibrium. The framework is compatible with both Cartesian and spherical-polar geometries—utilizing non-uniform grid spacing—and incorporates static (SMR) and adaptive mesh refinement to optimize computational efficiency. To address the inherent challenges of angular momentum conservation in spherical-polar coordinates, we implement a robust and consistent “passive scalar angular momentum algorithm” (PSAMA). Domain decomposition is managed through both Z-order and Hilbert space-filling curves to ensure scalability. The code has been rigorously verified against a suite of standard benchmarks and newly designed test cases specifically intended to diagnose the non-linear coupling between gas dynamics, intricate EoS, radiation transport, and angular momentum conservation.

*Keywords:* Hydrodynamical simulations (767) — Astronomical instrumentation (799)

### 1. INTRODUCTION

Astrophysical fluids are inherently multiphysics, multiscale, and highly nonlinear. They often span vast dynamical ranges in density and temperature, involving non-ideal processes such as phase transitions (e.g., ionization and dissociation). This complexity presents a significant modeling challenge, as the resulting equations of state (EoS) become highly intricate and non-linear. Furthermore, treating phase transitions across diverse physical conditions requires a rigorous thermodynamic framework, which is often coupled with radiation transport—introducing further computational com-

plications. Examples of such phenomena are ubiquitous, including type II supernovae (SNe) (Popov 1993; Smith 2017; Fang et al. 2025), dwarf novae (Lasota 2001; Hameury 2020), luminous red novae (LRNe) (Tylenda et al. 2011; Chen & Ivanova 2024; Chen 2025), common envelope evolution (CEE) (Ivanova et al. 2013; Moreno et al. 2022; Vetter et al. 2024), and star/planetary formation (Larson 1969; Bhandare et al. 2018; Chen & Bai 2022). Despite their importance, there remains a lack of multi-dimensional computational tools capable of simultaneously handling complex EoS and radiation transport. This deficiency motivates the development of a new astrophysical fluid dynamics code to bridge this gap.

We begin with the equation of radiative transfer—a 6D integro-differential equation dependent on spatial coordinates, angles, and frequency (Mihalas & Mihalas 1984; Castor 2004). It is customary to take angular moments of this equation to reduce its dimension-

Corresponding author: Zhuo Chen (陈卓)  
 chenzhuo\_astro@mail.tsinghua.edu.cn

Corresponding author: Xue-Ning Bai (白雪宁)  
 xbai@mail.tsinghua.edu.cn

ality. The simplest model for radiation transport involves taking the zeroth moment under the flux-limited-diffusion (FLD) approximation (Levermore & Pomraning 1981). FLD assumes a closure relation between radiation flux and radiation energy that transitions from diffusion to free-streaming between the optically thick and thin regimes. While the FLD equation generally requires implicit solvers (see Section 3.2 for details), it has been widely adopted in various radiation hydrodynamic (RHD) codes (e.g. Kolb et al. 2013; Ramsey & Dullemond 2015; Colombo et al. 2019). However, a primary drawback of the FLD approximation is its inability to properly capture the anisotropy of radiation transport (e.g., shadows) and its potential for inaccuracy at intermediate optical depths (Davis et al. 2014).

Improvements can be achieved by integrating the radiative transfer equation through both the zeroth and first moments, closing the system with the M1 approximation (Levermore 1984; Dubroca & Feugeas 1999). This two-moment formulation is hyperbolic, with characteristic wave speeds approaching the speed of light (Skinner & Ostriker 2013), which can impose stringent constraints on the timestep. Consequently, the M1 approximation is often paired with the reduced speed of light approximation (RSLA) (Gnedin & Abel 2001; Skinner & Ostriker 2013) and an explicit solver. However, the RSLA can violate energy conservation (Melon Fuksman et al. 2021; Wibking & Krumholz 2022). While the M1 approximation effectively captures shadow effects (González et al. 2007; Skinner & Ostriker 2013; Kannan et al. 2019; Bloch et al. 2021; Melon Fuksman et al. 2021; Wibking & Krumholz 2022), it fails in “cross-beam” scenarios (Jiang et al. 2012; Jiang 2021) because the closure relation cannot represent beams originating from multiple directions simultaneously.

The most accurate approach involves directly solving the radiative transfer equation across a discrete set of solid angles. This method provides superior local closure relations between the radiation pressure tensor and radiation energy density, leading to the variable Eddington tensor (VET) method (Davis et al. 2012; Jiang et al. 2012). Recently, it has become feasible to evolve the full radiative transfer equation coupled with hydrodynamics (Jiang 2021; Ma et al. 2025). The primary disadvantage of these approaches is their high computational cost compared to FLD or M1 approximations; maintaining high precision of energy conservation often requires additional iterations, further reducing computational efficiency.

Regardless of the approximation used, proper treatment of the coupling between radiation and gas energy is essential for conservation. This coupling is typically so

strong that the thermodynamic equations become stiff ordinary differential equations (ODEs) (Colombo et al. 2019) requiring implicit solutions. Furthermore, a complex EoS can become highly nonlinear as gas temperatures fall in the range of phase transitions, complicating the implicit solvers. Because local thermodynamics are also coupled to non-local radiation transport, the system is typically solved via a fully implicit scheme (Kolb et al. 2013) or an implicit-explicit (IMEX) scheme (Wibking & Krumholz 2022), depending on the transport solver.

In this work, we introduce *Guangqi* (光启)<sup>1</sup>, a new two-dimensional (2D) grid-based RHD code designed to handle general EoS. *Guangqi* is a finite-volume Godunov code compatible with Cartesian and non-uniform spherical polar coordinates; in the latter, it is specifically designed to precisely conserve angular momentum. To maintain high accuracy in energy conservation while minimizing computational overhead, we adopt the FLD approximation. The equations are coupled with a general EoS, and the system is solved fully implicitly. To validate the code, we have devised a suite of numerical tests that solve RHD and EoS concurrently for diagnostic purposes. Currently, *Guangqi* is configured to solve the RHD equations using a hydrogen ( $H_2$ ,  $H$ ,  $H^+$ , and  $e^-$ ) and helium ( $He$ ,  $He^+$ ,  $He^{2+}$ , and  $e^-$ ) EoS (Chen & Ivanova 2024) based on the Saha equations, assuming local thermodynamic equilibrium (LTE). We have also implemented adaptive mesh refinement (AMR) to facilitate simulations with large dynamical ranges. This new 2D code is ideally suited for long-term axisymmetric astrophysical problems involving complex thermodynamics and optically thick regions, such as CEE, LRNe, SNe, and star/planet formation. A new simple code can also offer an ideal testbed for novel algorithms, such as the radiation hydrodynamics with a complex EoS and the “passive scalar angular momentum algorithm” (PSAMA) that will be presented in this paper.

The remainder of this paper is organized as follows. Section 2 details the relevant physics and governing equations. Section 3 describes our numerical methodology. Section 4 introduces the domain decomposition strategy for parallelization. We present numerical test results and comparisons against known solutions in Section 5. Finally, we provide a summary and concluding remarks in Section 6.

## 2. THE GENERAL FORMALISM

<sup>1</sup> We choose the name as a tribute to Xu Guangqi (徐光启), a mathematician and astronomer who collaborated with Matteo Ricci; the name also translates to “enlightened by light” in Chinese.

Guangqi solves the 2D time-dependent radiation hydrodynamic equations with a general EoS. The RHD governing equations in the conservative form are,

$$\frac{\partial \rho}{\partial t} + \nabla \cdot (\rho \vec{v}) = 0, \quad (1)$$

$$\frac{\partial(\rho \vec{v})}{\partial t} + \nabla \cdot (\rho \vec{v} \vec{v} + p \mathbf{I}) = \rho \vec{f}, \quad (2)$$

$$\frac{\partial E}{\partial t} + \nabla \cdot [\vec{v}(E + p)] = G^0 + S_g + \rho \vec{f} \cdot \vec{v}, \quad (3)$$

$$\frac{\partial E_r}{\partial t} + \nabla \cdot (E_r \vec{v}) + \nabla \cdot \vec{F}_r = -G^0, \quad (4)$$

where  $\rho$ ,  $\vec{v}$ ,  $E$ ,  $p \mathbf{I}$ , and  $\vec{f}$  are the density, velocity, gas total energy density, pressure tensor, and external force such as gravity), respectively. The total energy includes the kinetic energy and internal energy,

$$E = \rho \left( \frac{v^2}{2} + \epsilon \right), \quad (5)$$

$$\epsilon = \epsilon(\rho, T_g), \quad (6)$$

where  $v$ ,  $\epsilon$ ,  $T_g$  are the speed, specific internal energy, and gas temperature,  $S_g$  represents external heating or cooling source terms (e.g., irradiation). For the gas consisting of  $k$  species, with the number density of each species  $i$  being  $n_i$ , and the mass of each gas molecule/atom being  $m_i$ , we simply have,

$$\rho = \sum_{i=1}^k n_i m_i, \quad (7)$$

$$p = \sum_{i=1}^k n_i k_b T_g, \quad (8)$$

where  $k_b$  is the Boltzmann constant, and the pressure  $p$  is given by the ideal gas law. Equation 6 is a general EoS and can be nonlinear for realistic gas, where we assume that all the species are in LTE and  $n_i$  can be solved with Saha equations. Chen et al. (2019) introduced a fast and accurate EoS solver to solve the Saha equations of hydrogen species, which we adopt in this work.

The radiation-related quantities are the radiation energy density  $E_r$ , and radiation flux  $\vec{F}_r$ , measured in the lab frame, and the radiation-matter coupling strength  $G^0$ . They are defined as,

$$E_r = \frac{1}{c} \int I_\nu d\omega d\nu, \quad (9)$$

$$\vec{F}_r = \int I_\nu \hat{\Omega} d\omega d\nu, \quad (10)$$

$$G^0 = \rho c \kappa_P E_r - \eta, \quad (11)$$

where  $\kappa_P$  and  $\eta$  are the Planck mean opacity and emissivity measured in the co-moving frame,  $\omega$ ,  $\hat{\Omega}$ , and  $\nu$

are the solid angle, unit vector in the direction of the solid angle, and frequency. The specific intensity  $I_\nu$  is the fundamental quantity in the radiative transfer which depends on the coordinate, solid angle, and frequency. Its value can be obtained by solving the radiative transfer equation (Mihalas & Mihalas 1984; Castor 2004), which can be quite complicated. For convenience, we can equivalently express radiation energy density in terms of an effective radiation temperature (which is rigorous when radiation is isotropic and black body),

$$E_r = a_R T_{\text{rad}}^4, \quad (12)$$

where  $a_R$  is the radiation constant.

To calculate the radiation flux  $\vec{F}_r$ , we employ the FLD approximation for simplicity, given by (Levermore & Pomraning 1981)

$$\vec{F}_r = \frac{-c\lambda}{\kappa_R \rho} \nabla E_r \equiv -D \nabla E_r \quad (13)$$

where  $D$  is the diffusion coefficient,  $\kappa_R$  is the Rossland mean opacity. In the FLD approximation,  $\lambda$  is the flux limiter which should have the following asymptotic behaviors,

$$\frac{c\lambda}{\kappa_R \rho} \nabla E_r \rightarrow \begin{cases} \frac{c}{3\kappa_R \rho} \nabla E_r & \text{optically thick} \\ c E_r & \text{optically thin} \end{cases} \quad (14)$$

In this paper, the flux limiter we choose is based on Minerbo (1978),

$$\lambda = \begin{cases} \frac{2}{3 + \sqrt{9 + 12\mathcal{R}^2}} & 0 \leq \mathcal{R} \leq \frac{3}{2} \\ \frac{1}{1 + \mathcal{R} + \sqrt{1 + 2\mathcal{R}}} & \frac{3}{2} < \mathcal{R} < \infty \end{cases} \quad (15)$$

where

$$\mathcal{R} = \frac{|\nabla E_r|}{\kappa_R \rho E_r}. \quad (16)$$

Other flux limiters are also available (Levermore & Pomraning 1981; Kley 1989).

The Rosseland mean opacity and Planck mean opacity are defined as

$$\frac{1}{\kappa_R} = \frac{\int I_\nu / \kappa_\nu d\nu}{\int I_\nu d\nu}, \quad (17)$$

$$\kappa_P = \frac{\int \kappa_\nu I_\nu d\nu}{\int I_\nu d\nu} \quad (18)$$

where  $\kappa_\nu$  is the opacity at frequency  $\nu$ . These mean opacities are often tabulated as a function of radiation temperature  $T_{\text{rad}}$ . In Equation 11, the emissivity is by default taken to be,

$$\eta = \kappa_e \rho c a_R T_g^4, \quad (19)$$

where  $\kappa_e$  is the emission opacity measured in the co-moving frame. In more realistic cases,  $\eta$  can be tabulated (e.g. Colombo et al. 2019). In the test problems used in this work, we assume  $\kappa_e = \kappa_p$  for simplicity.

### 3. NUMERICAL SCHEME

We solve the system of general EoS radiation hydrodynamic equations using a two-step operator-splitting approach. In the first step, the pure hydrodynamic equations are resolved using a general EoS Riemann solver (see Section 3.1.1). In the second step, we solve the radiation transport equations under the FLD approximation, concurrently accounting for the thermodynamic coupling with the general EoS. This split allows for the use of robust hyperbolic solvers for the fluid dynamics while employing implicit methods for the stiff radiation-matter coupling.

#### 3.1. Hydrodynamic solvers

##### 3.1.1. Basic algorithm for general EoS hydrodynamics

Firstly, we solve the hydrodynamic equations and a realistic EoS with a general HLLC Riemann solver (Chen et al. 2019), or a classic HLLC Riemann solver in the case of  $\gamma$ -law gas (Batten et al. 1997). In this section, we assume a uniform grid in Cartesian coordinates and focus on describing the necessary steps to solve the equations in 2D by the MUSCL scheme (van Leer 1974) which has a second-order spatial and temporal accuracy. A novel algorithm for spherical polar coordinates is described in Section 3.1.2.

The hydrodynamic equations are expressed in compact conservation form, temporarily omitting the energy source terms  $S_g$  and  $G^0$ :

$$\frac{\partial U}{\partial t} + \frac{\partial F}{\partial x} + \frac{\partial G}{\partial y} = S, \quad (20)$$

where,  $U$ ,  $F$ ,  $G$ , and  $S$  are the conserved quantities, fluxes in the  $x$  and  $y$  directions, and the source term due to any external forces, respectively, i.e.,

$$U = \begin{bmatrix} \rho \\ \rho v_x \\ \rho v_y \\ E \end{bmatrix}, \quad F = \begin{bmatrix} \rho v_x \\ \rho v_x^2 + p \\ \rho v_x v_y \\ v(E + p) \end{bmatrix}, \quad G = \begin{bmatrix} \rho v_y \\ \rho v_x v_y \\ \rho v_y^2 + p \\ v(E + p) \end{bmatrix}, \quad (21)$$

$$S = \begin{bmatrix} 0 \\ \rho f_x \\ \rho f_y \\ \rho(f_x v_x + f_y v_y) \end{bmatrix}.$$

The primitive quantities in cell  $(i, j)$  are denoted by the vector  $W_{i,j}^n = [\rho, v_x, v_y, p]^T$ . Our primary strategy is

to solve Equation 20 in a directionally unsplit manner. Specifically, we treat the hyperbolic flux divergence and the source terms as:

$$\frac{\partial U}{\partial t} = -\frac{\partial F}{\partial x} - \frac{\partial G}{\partial y}, \quad (22)$$

$$\frac{\partial U}{\partial t} = S. \quad (23)$$

To advance the system from time step  $n$  to  $n + 1$ , we employ the following second-order predictor-corrector (midpoint) procedure:

1. We perform piecewise linear reconstruction of the primitive quantities  $W_{i,j}^n$  at all cell interfaces using a slope limiter (SL) (Zou 2021). This yields the interface states  $W_{i-\frac{1}{2},j,R}^n$  and  $W_{i+\frac{1}{2},j,L}^n$ , where L and R denote the left and right sides of the interface, respectively. A similar procedure is applied along the  $y$ -axis. The limited difference  $\delta W_{i,j}^n$  along the  $x$ -direction is calculated as:

$$W_{i-\frac{1}{2},j,R}^n = W_{i,j} - \delta W_{i,j}^n / 2, \quad (24)$$

$$W_{i+\frac{1}{2},j,L}^n = W_{i,j} + \delta W_{i,j}^n / 2, \quad (25)$$

$$\delta W_{i,j}^n = \text{SL}(\bar{\delta} W_{i,j,L}^n, \bar{\delta} W_{i,j,C}^n, \bar{\delta} W_{i,j,R}^n), \quad (26)$$

where  $\delta W_{i,j}^n$  denotes the limited difference and is calculated from the left, right, and central differences,

$$\bar{\delta} W_{i,j,L}^n = W_{i,j} - W_{i-1,j}^n \quad (27)$$

$$\bar{\delta} W_{i,j,R}^n = W_{i+1,j}^n - W_{i,j}^n \quad (28)$$

$$\bar{\delta} W_{i,j,C}^n = (W_{i+1,j}^n - W_{i-1,j}^n) / 2 \quad (29)$$

To ensure numerical robustness—particularly in the presence of complex EoS and curvilinear coordinates—Guangqi employs the minmod limiter as its default.

2. Solve the general EoS Riemann problems with an HLLC Riemann solver (Chen et al. 2019) at all interfaces given  $W_{i\pm\frac{1}{2},j,L/R}^n$  and  $W_{i,j\pm\frac{1}{2},L/R}^n$  to obtain the fluxes  $F_{i\pm\frac{1}{2},j}^n$  and  $G_{i,j\pm\frac{1}{2}}^n$  at the  $x$  and  $y$  interfaces. In the mean time, save the wave speeds of the Riemann problems at all interfaces.
3. Estimate the hydrodynamic timestep  $\Delta t$  based on the Courant-Friedrichs-Lowy (CFL) condition (Courant et al. 1928),

$$\Delta t = \text{CFL} \cdot \min \left\{ \min \left( \frac{\Delta x}{v_x} \right), \min \left( \frac{\Delta y}{v_y} \right) \right\}, \quad (30)$$

where  $\Delta x$  and  $\Delta y$  are the cell size in  $x$  and  $y$  directions, and  $v_x$  and  $v_y$  are the wave speeds of the

Riemann solution at the cells'  $x$  and  $y$  directions' interfaces. Stability requires the CFL number to be  $\leq 1$  in 1D problems and  $\leq 0.5$  in 2D problems. This criterion also applies to the non-uniform grid.

4. Integrate the Equation 22 for half a time-step  $\Delta t/2$  by applying flux divergence law

$$\bar{U}_{i,j}^{n+\frac{1}{2}} - U_{i,j}^n = \frac{\Delta t(F_{i-\frac{1}{2},j}^n - F_{i+\frac{1}{2},j}^n)}{2\Delta x} + \frac{\Delta t(G_{i,j-\frac{1}{2}}^n - G_{i,j+\frac{1}{2}}^n)}{2\Delta y}. \quad (31)$$

Integrate the Equation 23 for half a time-step  $\Delta t/2$

$$U_{i,j}^{n+\frac{1}{2}} - \bar{U}_{i,j}^{n+\frac{1}{2}} = \frac{\Delta t S_{i,j}^n}{2}. \quad (32)$$

5. Convert  $U_{i,j}^{n+\frac{1}{2}}$  to  $W_{i,j}^{n+\frac{1}{2}}$ , reconstruct  $W_{i,j}^{n+\frac{1}{2}}$  with the same slope limiter to obtain  $W_{i\pm\frac{1}{2},j,\text{L/R}}^{n+\frac{1}{2}}$  and  $W_{i,j\pm\frac{1}{2},\text{L/R}}^{n+\frac{1}{2}}$ .

6. Solve the Riemann problems at all interfaces to obtain  $F_{i\pm\frac{1}{2},j}^{n+\frac{1}{2}}$  and  $G_{i,j\pm\frac{1}{2}}^{n+\frac{1}{2}}$ .

7. Apply flux divergence law to calculate  $\bar{U}^{n+1}$ ,

$$\bar{U}_{i,j}^{n+1} - U_{i,j}^n = \frac{\Delta t(F_{i-\frac{1}{2},j}^{n+\frac{1}{2}} - F_{i+\frac{1}{2},j}^{n+\frac{1}{2}})}{\Delta x} + \frac{\Delta t(G_{i,j-\frac{1}{2}}^{n+\frac{1}{2}} - G_{i,j+\frac{1}{2}}^{n+\frac{1}{2}})}{\Delta y}, \quad (33)$$

and integrate the Equation 23 for  $\Delta t$  from the state of time step  $n$ .

$$U_{i,j}^{n+1} - \bar{U}_{i,j}^{n+1} = \Delta t S_{i,j}^{n+\frac{1}{2}}. \quad (34)$$

8. Convert  $U_{i,j}^{n+1}$  to  $W_{i,j}^{n+1}$ .

We have not included boundary communications here. They will be discussed in Section 4.2, where additional communications associated with static mesh refinement (SMR)/AMR will also be addressed.

### 3.1.2. Extension to spherical-polar coordinates: the PSAMA

Astrophysical simulations in spherical-polar coordinates frequently involve systems dominated by central gravity, where the precise conservation of angular momentum is paramount. We introduce a novel numerical scheme that conserves angular momentum to machine precision while maintaining superior numerical stability compared to conventional methods. The derivation

here assumes azimuthal symmetry (commensurate with the 2D nature of *Guangqi*), but generalization to 3D is straightforward. We first write down the hydrodynamic equations in spherical polar coordinates,

$$\frac{\partial \rho}{\partial t} + \frac{1}{r^2} \frac{\partial(r^2 \rho v_r)}{\partial r} + \frac{1}{r \sin \theta} \frac{\partial(\sin \theta \rho v_\theta)}{\partial \theta} = 0, \quad (35)$$

$$\frac{\partial(\rho v_r)}{\partial t} + \frac{1}{r^2} \frac{\partial[r^2(\rho v_r^2 + p)]}{\partial r} + \frac{1}{r \sin \theta} \frac{\partial(\sin \theta \rho v_r v_\theta)}{\partial \theta} = \rho g_r + \frac{2p}{r} + \frac{\rho(v_\theta^2 + v_\phi^2)}{r}, \quad (36)$$

$$\frac{\partial(\rho v_\theta)}{\partial t} + \frac{1}{r^2} \frac{\partial(r^2 \rho v_r v_\theta)}{\partial r} + \frac{1}{r \sin \theta} \frac{\partial[\sin \theta(\rho v_\theta^2 + p)]}{\partial \theta} = \frac{\cot \theta(\rho v_\phi^2 + p) - \rho v_r v_\theta}{r}, \quad (37)$$

$$\frac{\partial(\rho v_\phi)}{\partial t} + \frac{1}{r^2} \frac{\partial(r^2 \rho v_r v_\phi)}{\partial r} + \frac{1}{r \sin \theta} \frac{\partial(\sin \theta \rho v_\theta v_\phi)}{\partial \theta} = \frac{-\rho v_r v_\phi}{r} - \frac{\cot \theta \rho v_\theta v_\phi}{r}, \quad (38)$$

$$\frac{\partial E}{\partial t} + \frac{1}{r^2} \frac{\partial[r^2(E + p)v_r]}{\partial r} + \frac{1}{r \sin \theta} \frac{\partial[\sin \theta(E + p)v_\theta]}{\partial \theta} = \rho g_r v_r. \quad (39)$$

The left-hand side (LHS) of Equations 35–39 represents the system in linear-momentum conservative form, which can be resolved directly using a standard Riemann solver at cell interfaces. The complete evolution is achieved by integrating the source terms on the right-hand side (RHS) following the second-order predictor-corrector steps described in Equations 32 and 34. However, due to finite spatial resolution, the non-zero source terms—particularly those in the  $\phi$ -momentum equation—generally lead to a violation of the underlying conservation laws. Specifically, the conservation of linear momentum in the  $\phi$ -direction and the resulting angular momentum along the polar axis are not guaranteed due to the geometric source terms in Equation 38.

A common remedy is to post-process the linear momentum flux after the Riemann solver stage to reflect angular momentum conservation in curvilinear coordinates (Mignone et al. 2007; Skinner & Ostriker 2010; Ju et al. 2016, 2017). Nevertheless, this modification does not recover the true solution of an angular-momentum-based Riemann problem. Furthermore, in the modification, the conserved quantities is changed from the linear momentum in the Riemann problem solution to the angular momentum that is used in the flux divergence law, which introduces an inconsistency (see Appendix A for further discussions). To overcome the tension between the angular momentum conservation and consistent energy evolution when using a Riemann solver, we propose

a new scheme, which we term “passive scalar angular momentum algorithm (PSAMA)” as follows.

We first rewrite Equation 38 in the angular momentum conservation form,

$$\frac{\partial(\rho l)}{\partial t} + \frac{1}{r^2} \frac{\partial(r^2 \rho v_r l)}{\partial r} + \frac{1}{r \sin \theta} \frac{\partial(\rho v_\theta l \sin \theta)}{\partial \theta} = \frac{\partial(\rho l)}{\partial t} + \nabla \cdot (\rho \vec{v} l) = 0 \quad (40)$$

where  $l = r \sin \theta v_\phi = (r \sin \theta)^2 \Omega$  is the specific angular momentum along the polar axis and  $\Omega$  is the angular frequency. Equation 40 indicates that the angular momentum is a passive scalar. Then, we split the total energy into two parts in the following way,

$$E = \underbrace{\rho \left( \epsilon_g + \frac{v_r^2 + v_\theta^2}{2} \right)}_{E'} + \underbrace{\frac{\rho l^2}{2(r \sin \theta)^2}}_{e_{k\phi}} \quad (41)$$

where  $e_{k\phi}$  is the kinetic energy in the  $\phi$  direction and  $E'$  is the sum of the internal energy and the kinetic energy in  $r$  and  $\theta$  direction. We adapt Equation 39 correspondingly,

$$\frac{\partial E'}{\partial t} + \frac{1}{r^2} \frac{\partial[r^2(E' + p)v_r]}{\partial r} + \frac{1}{r \sin \theta} \frac{\partial[\sin \theta(E' + p)v_\theta]}{\partial \theta} + \frac{\partial e_{k\phi}}{\partial t} + \nabla \cdot (e_{k\phi} \vec{v}) = \rho g_r v_r. \quad (42)$$

The key is to express  $\partial e_{k\phi} / \partial t + \nabla \cdot (e_{k\phi} \vec{v})$  in terms of known variables. We put the derivation in Appendix B. The result is,

$$\frac{\partial e_{k\phi}}{\partial t} + \nabla \cdot (e_{k\phi} \vec{v}) = -\rho \vec{f}_\Omega \cdot \vec{v}, \quad (43)$$

where  $\vec{f}_\Omega = r \Omega^2 \sin \theta [\sin \theta, \cos \theta, 0]^T$ . Substitute Equation 43 into 42, and move the source term to the RHS, we obtain the energy transport equation,

$$\frac{\partial E'}{\partial t} + \nabla \cdot [(E' + p) \vec{v}] = \rho g_r v_r + \rho \vec{f}_\Omega \cdot \vec{v}. \quad (44)$$

To summarize succinctly, we outline the main steps for proceeding a half timestep, which corresponds to steps 1 to 5 in Section 3.1.1.

1. Reconstruct the primitive quantities. Use  $\Omega$  to do the reconstruction of  $l$ .
2. Solve the Riemann problems of  $[\rho, \rho v_r, \rho v_\theta, E']$  in the  $r$  and  $\theta$  directions, i.e., Equation 35, 36, 37, and 44 in the same manner as in the Cartesian coordinate.
3. Estimate the timestep  $\Delta t$ .

4. Apply the flux divergence law to the conserved quantities  $[\rho, \rho v_r, \rho v_\theta, E']$  and the angular momentum  $\rho l$ . Add the second order source terms as described in Appendix C according to the operator unsplit manner introduced in Section 3.1.1.
5. Obtain the half timestep state  $[\rho, \rho v_r, \rho v_\theta, E']$  and  $\Omega$  by converting the conserved quantities to the primitive quantities.

Step 6 to 8 follow the same procedures.

PSAMA ensures the precise conservation of angular momentum in spherical-polar coordinates while maintaining consistency between the linear-momentum-based Riemann solver and the flux divergence law. This consistency is achieved at the expense of an additional source term,  $\rho \vec{f}_\Omega \cdot \vec{v}$ , on the right-hand side (RHS) of Equation 44, which formally compromises exact energy conservation. However, in the presence of gravitational source terms and implicit radiation transport, absolute energy conservation is already numerically constrained by the convergence limits of iterative solvers. We therefore advocate for PSAMA as a more robust and internally consistent algorithm for rotating flows. Its effectiveness is demonstrated through a suite of numerical benchmarks in Section 5.3.2.

### 3.2. FLD Radiation transport and implicit method

The second main step is to solve the equation of radiation transport with the FLD approximation, coupled with the equation of gas thermodynamics,

$$\frac{\partial E_r}{\partial t} + \nabla \cdot (v E_r) - \nabla \cdot (D \frac{\partial E_r}{\partial x}) = G^0 \quad (45)$$

$$C_V \frac{\partial T_g}{\partial t} = -G^0 + S_g \quad (46)$$

where

$$C_V = \frac{\partial e_g(\rho, T_g)}{\partial T_g} \quad (47)$$

is the heat capacity per unit volume at  $(\rho, T_g)$ .

The diffusion term in Equation 45 imposes a stringent constraint on the simulation timestep if treated explicitly, as the stability criterion  $\delta t < \min(\Delta x^2 / (4D))$  must be satisfied. According to Fick’s law,  $D \sim v L_d$ , where  $v$  is the characteristic speed and  $L_d$  is the diffusion length scale. In optically thin regimes, the diffusion coefficient scales as  $D \sim c \lambda_{\text{mfp}}$ , where  $\lambda_{\text{mfp}}$  is the photon mean free path. Consequently, the required explicit stability limit  $\delta t$  becomes orders of magnitude smaller than the hydrodynamic timestep  $\Delta t$  governed by the CFL condition (i.e.,  $\delta t \ll \Delta t$ ). To circumvent this severe constraint, a fully implicit scheme is required to solve Equations 45 and 46. We therefore adopt a standard backward Euler discretization for the radiation transport.

### 3.2.1. Uniform Cartesian grid

We start with the algorithm to solve the problem in a uniform Cartesian grid with  $N_1 \times N_2$  cells. The algorithm for SMR/AMR grid will be discussed in Section 3.2.2. We discretize equations 45 and 46 using the backward Euler method,

$$\begin{aligned} \phi_1 E_{i,j-1}^{n+1} + \phi_2 T_{i,j-1}^{n+1} + \phi_3 E_{i-1,j}^{n+1} + \phi_4 T_{i-1,j}^{n+1} \\ + \phi_5 E_{i,j}^{n+1} + \phi_6 T_{i,j}^{n+1} + \phi_7 E_{i+1,j}^{n+1} + \phi_8 T_{i+1,j}^{n+1} \\ + \phi_9 E_{i,j+1}^{n+1} + \phi_{10} T_{i,j+1}^{n+1} = \phi_{11}, \end{aligned} \quad (48)$$

$$\begin{aligned} \psi_1 E_{i,j-1}^{n+1} + \psi_2 T_{i,j-1}^{n+1} + \psi_3 E_{i-1,j}^{n+1} + \psi_4 T_{i-1,j}^{n+1} \\ + \psi_5 E_{i,j}^{n+1} + \psi_6 T_{i,j}^{n+1} + \psi_7 E_{i+1,j}^{n+1} + \psi_8 T_{i+1,j}^{n+1} \\ + \psi_9 E_{i,j+1}^{n+1} + \psi_{10} T_{i,j+1}^{n+1} = \psi_{11}, \end{aligned} \quad (49)$$

where we have omitted the subscripts  $g$  in  $T_g$  and  $r$  in  $E_r$  for brevity. Equations 48 and 49 consist of a large sparse linear system (linear system, hereafter)  $\mathbb{A}x = \mathbf{b}$ , where  $\mathbb{A}$  is the matrix of the linear system,  $x = [E_{i,j}, T_{i,j}]^T$  that spans over the entire grid ( $2N_1N_2$  variables to be solved), and  $\mathbf{b}$  represents the right-hand side of the linear system.

To assemble the linear system, we need to calculate all the  $\phi$  and  $\psi$  coefficients. First, we approximate the non-linear term  $T_g^4$  in  $G^0$  with Taylor's expansion to the first order,

$$(T_g^{n+1})^4 \approx 4(T_g^n)^3 T_g^{n+1} - 3(T_g^n)^4. \quad (50)$$

Then, we explicitly calculate the time averaged advection term. Specifically,

$$\nabla \cdot (v E_r) = \nabla \cdot (\rho v \frac{E_r}{\rho}) = -S_{\text{adv}}. \quad (51)$$

We observe that the mass flux  $\rho v$  at the cell interfaces corresponds directly to the solution of the mass conservation equation in the Riemann problem, which we denote as  $f_{i \pm 1/2, j}$  and  $f_{i, j \pm 1/2}$ . Consequently, by assuming that the specific radiation energy,  $e_r = E_r/\rho$ , remains constant within each cell, the advection term for the  $(i, j)$  cell can be discretized as follows:

$$\begin{aligned} S_{\text{adv}} = g_{i-1/2,j} f_{i-1/2,j} e_{r,i-1/2,j} - g_{i+1/2,j} f_{i+1/2,j} e_{r,i+1/2,j} \\ + g_{i,j-1/2} f_{i,j-1/2} e_{r,i,j-1/2} - g_{i,j+1/2} f_{i,j+1/2} e_{r,i,j+1/2}, \end{aligned} \quad (52)$$

where

$$g_{i \pm 1/2, j \pm 1/2} = dS_{i \pm 1/2, j \pm 1/2} / dV_{i,j}, \quad (53)$$

is the geometric factor, and  $dS_{i \pm 1/2, j \pm 1/2}$  and  $dV_{i,j}$  are the corresponding cell's bounding interface area and volume. The specific radiation energy  $e_{r,i \pm 1/2, j \pm 1/2}$  can be determined by the upwind condition.

On a uniform grid, the diffusion coefficient  $D$  is calculated at all interfaces between neighboring cells. Taking the interfaces perpendicular to the  $x$ -axis as an example, the coefficient is discretized as:

$$D_{i+1/2} = \frac{-c\lambda(\mathcal{R})}{(\kappa_R \rho)_{i+1/2}}, \quad (54)$$

where  $(\kappa_R \rho)_{i+1/2} = \sigma_{i+1/2}$  is an interface value and should be interpolated from the cell center value. To determine the dimensionless gradient  $\mathcal{R}$ , which is required for the flux limiter  $\lambda(\mathcal{R})$ , we utilize the spatial average of the radiation energy density from the adjacent cells to estimate the interface value  $E_{r,i+1/2}$ .

The non-zero elements of the linear system are:

$$\phi_1 = -\alpha_{i,j-1/2} g_{i,j-1/2} D_{i,j-1/2}^n, \quad (55)$$

$$\phi_3 = -\alpha_{i-1/2,j} g_{i-1/2,j} D_{i-1/2,j}^n, \quad (56)$$

$$\phi_5 = 1 - \phi_1 - \phi_3 - \phi_7 - \phi_9 + \beta_P^n \quad (57)$$

$$\phi_6 = -4\beta_e^n a_R (T_{i,j}^n)^3, \quad (58)$$

$$\phi_7 = -\alpha_{i+1/2,j} g_{i+1/2,j} D_{i+1/2,j}^n, \quad (59)$$

$$\phi_9 = -\alpha_{i,j+1/2} g_{i,j+1/2} D_{i,j+1/2}^n, \quad (60)$$

$$\phi_{11} = E_{r,i,j}^n - 3\beta_e a_R (T_{i,j}^n)^4 + (S_{\text{adv}} + S_g) \delta t \quad (61)$$

$$\psi_5 = -\beta_P^n \quad (62)$$

$$\psi_6 = C_V + 4\beta_e a_R (T_{i,j}^n)^3 \quad (63)$$

$$\psi_{11} = C_V T_{i,j} + 3\beta_e a_R (T_{i,j}^n)^4 \quad (64)$$

where  $\beta_P = \kappa_P \rho c \delta t$ ,  $\beta_e = \kappa_e \rho c \delta t$ , and  $\alpha_{i \pm 1/2, j \pm 1/2}$  is related to the spacing between the neighboring cells, for example,

$$\alpha_{i+1/2,j} = \delta t / (x_{i+1,j} - x_{i,j}), \quad (65)$$

where  $x_{i,j}$  is volume center. Here  $\delta t \leq \Delta t$  is the timestep of the radiation transport step. When  $\delta t = \Delta t$ , we integrate the radiation transport equation in a single time step. However, the gas and radiation energy coupling strength may be very strong and the  $T_g$  may be drastically different from the  $T_{\text{rad}}$  at shocks, making the local thermodynamics a stiff problem. In addition,  $C_V$  of a realistic gas may vary rapidly with temperature during phase transitions and can be another stiff term. As an example, Figure 1 shows  $C_V/\rho$  v.s.  $T_g$  of pure hydrogen gases at various densities.

The most straightforward recipe to handle the stiff problem is to reduce the integration timestep. In principle, we can split the integration of the radiation transport into sub-steps that is determined by

$$\delta t = \min(\Delta t_{\text{remain}}, \delta t_{\text{rad},i,j}) \quad (66)$$

$$\delta t_{\text{rad},i,j} = \bar{\delta} T_g \rho C_V / |G^0| \quad (67)$$

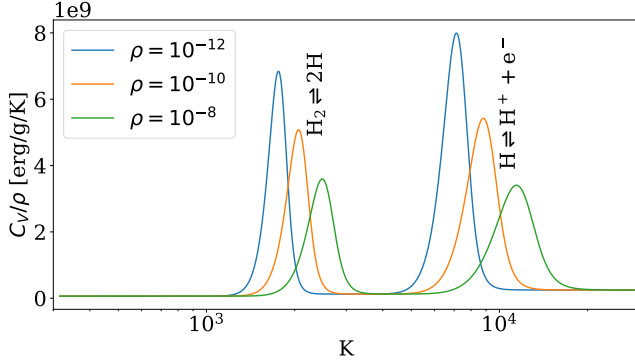


**Figure 1.** The specific heat capacity  $C_V/\rho$  of hydrogen gas as a function of temperature. The yellow and purple bands indicate the dissociation and ionization region, respectively, where the specific heat capacity shows rapid variations.

where  $\Delta t_{\text{remain}}$  is the remaining time of this hydro time step,  $\delta t_{\text{rad},i,j}$  is the time step limited by the radiation-matter coupling strength  $G^0$  at  $(i,j)$  cell, and  $\bar{\delta} < 0.1$  is the coefficient that controls the maximum temperature change between each sub-step. In practice, we can use a prescribed geometric series to determine the sub-timesteps,

$$\delta t_{i_{\text{sub}}} = \delta t_0 q_t^{i_{\text{sub}}-1}, \quad i_{\text{sub}} \in [1, n_{\text{sub}}] \quad (68)$$

$$\delta t_0 = \frac{\Delta t(1 - q_t)}{1 - q_t^{n_{\text{sub}}}}, \quad (69)$$

where  $1 < q_t < 2$  is the geometric factor and  $n_{\text{sub}}$  is total number of sub-cycles. The choice of  $q_t$  and  $n_{\text{sub}}$  are very problem dependent and should be explored by the users. We present several tests in Section 5.1.2.

The rank of the linear system (Equation 45 and 46) is  $2N_1N_2$ , and the number of non-zero elements are small compared to the number of zero elements. To solve the linear system efficiently, we employ the external package **Petsc**<sup>2</sup>, and use the GMRES iteration method (Saad & Schultz 1986). We have experimented with some classic preconditioners including the block Jacobi, incomplete LU, and LU preconditioners, and found that additive Schwarz preconditioner (PCASM<sup>3</sup>) is in general a good choice for the block structure computational domain. As an iterative solver, **Petsc** solves the linear system problem  $\mathbf{Ax} = \mathbf{b}$  approximately. We set the convergence criterion by the relative error  $\epsilon_r$  in the residual,

$$\|\mathbf{b} - \mathbf{Ax}_k\| < \epsilon_r \|\mathbf{b}\|, \quad (70)$$

where  $\|\cdot\|$  takes the 2-norm and  $k$  in the subscript is the iteration number.

Finally, we can calculate  $\vec{F}_r$  at interfaces as,

$$\vec{F}_{r,i+\frac{1}{2},j} = D_{i+\frac{1}{2},j}^n \sum_{i_{\text{sub}}} \frac{\alpha_{i+\frac{1}{2},j}^{i_{\text{sub}}}(E_{r,i+1,j}^{n,i_{\text{sub}}} - E_{r,i,j}^{n,i_{\text{sub}}})}{\Delta t} \quad (71)$$

where  $i_{\text{sub}}$  is the sub-cycle index.

We summarize the calculation steps in the radiation subsystem.

1. Calculate  $S_{\text{adv}}$  according to Equation 52 of all cells. Construct the series of  $\delta t_{i_{\text{sub}}}$  according to Equation 68.
2. Calculate  $g$ ,  $D$ , and  $\alpha$  and at all interfaces according to Equation 53, 54, and 65, respectively.
3. Calculate  $C_V$  of all cells.
4. Calculate  $\phi$  and  $\psi$  with Equation 55-64.
5. Assemble  $\mathbf{A}$  and  $\mathbf{b}$  of the linear system.
6. Solve the linear system problem with an iterative solver.
7. When  $i_{\text{sub}} < n_{\text{sub}}$ , update  $\alpha$  and go to step 3.
8. Calculate  $\vec{F}_r$  if needed.

### 3.2.2. Implicit algorithm with SMR/AMR

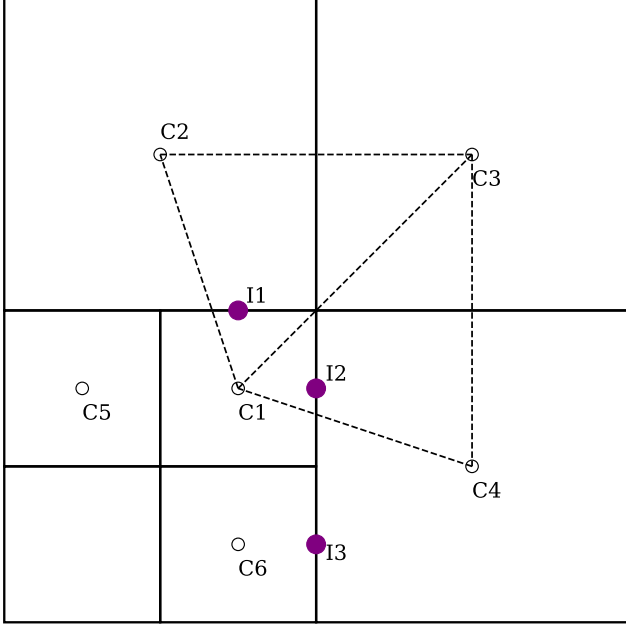
The major difference between a uniform grid and a grid with SMR/AMR in the radiation transport step is the topological relation between different levels. Thus, it leads to a more complex calculation of the diffusion coefficient  $D$ . As mentioned in Section 3.2.1, we need to calculate  $E_r$ ,  $\nabla E_r$ , and  $\kappa_R \rho$  at all the interfaces. In a grid with mesh refinement (Figure 2), the interface value is related to more neighbor cells.

Figure 2 shows refined cells in the bottom-left next to the coarser cells, where I1, I2, and I3 are at the interfaces with the finer cells. We can linearly interpolate  $E_r$  and  $\kappa_R \rho$  at C1, C2, and C3 to get  $E_r$ ,  $\nabla E_r$ , and  $\kappa_R \rho$  at I1, the same logic follows for I2 and I3. Then, the  $D$  of the finer cells at the level jumps can be calculated from the interpolated variables. However, the value of  $D$  for the coarser cells at the level jumps is more complicated.

In the AMR implementations described by Commerçon et al. (2011, 2014), a single  $D$  of the coarse cells at the level jumps is calculated with interpolated variables at the interfaces so that all cells have the same number of neighbors. The linear system is thus more regular with this topological configuration. However, there is a potential numerical inconsistency between the total fluxes crossing the fine cells and the flux crossing the coarse cell if they are using different  $D$ .

<sup>2</sup> [Petsc webpage](#)

<sup>3</sup> [Petsc PCASM webpage](#)



**Figure 2.** A mesh refinement structure showing refined cells in the bottom-left next to the unrefined cells. Values of interfaces (purple dots labeled I) and cell centers (black hollow circles) when there is a level difference.

Alternatively, one can adopt the “deferred synchronization” algorithm that solves the partitioned matrix across different refinement levels in a staggered manner (Howell & Greenough 2003; Zhang et al. 2011; Ramsey & Dullemond 2015). The load balancing suffers from this additional splitting and radiation transport is also splitted, i.e., the refined zone does not know the physical condition (optically thick/thin) of the coarse zone when it is being updated, vice versa.

Here, we let the coarse cells to communicate directly with the fine cells and solve the multilevel implicit radiation transport problem in a single matrix. Specifically, we send  $D$  at I2 and I3 to the coarse cell at C4, and C4 will have 5 neighboring cells (assuming other neighbors are the same level as C4). Correspondingly, the linear system of C4 has one additional non-zeros terms, and changes to

$$\begin{aligned} \phi_1 E_{i,j-1}^n + \phi_{3,C1} E_{i-1,j,C1}^n + \phi_{3,C6} E_{i-1,j,C6}^n + \\ + \phi_5 E_{i,j}^n + \phi_6 T_{i,j}^n + \phi_7 E_{i+1,j}^n + \phi_9 E_{i,j+1}^n = \phi_{11}. \end{aligned} \quad (72)$$

The presence of  $\phi_{3,C1} E_{i-1,j,C1}^n$  and  $\phi_{3,C6} E_{i-1,j,C6}^n$  enables the direct communication between C1, C4, and C6. Meanwhile, the fluxes between the fine and coarse cells are now more consistent.

#### 4. DOMAIN DECOMPOSITION AND COMMUNICATIONS

As an SMR/AMR code employing MPI parallelization, *Guangqi* manages complex data synchronization across multiple refinement levels and processor domains. Our 2D AMR framework utilizes a block-structured quad-tree data structure, a design philosophy shared with established codes such as *FLASH* (Fryxell et al. 2000), *AMRVAC* (Keppens et al. 2003), and *Athena++* (Stone et al. 2020).

The criteria for mesh refinement are highly problem-dependent; for a comprehensive list of representative criteria, we refer the reader to Bryan et al. (2014). Currently, to ensure simplicity and maximize parallel efficiency, *Guangqi* integrates all cells across different levels using a global time step  $\Delta t$ . While this approach simplifies the global synchronization of the monolithic radiation matrix, it presents challenges in multilevel configurations. Specifically, the small  $\Delta t$  required by the finest level effectively reduces the CFL number for the coarser grids, thereby introducing significant numerical diffusion. For simulations that prioritize the accurate advection of large-scale structures on the coarse grid, an adaptive, level-dependent timestep may be preferable (Bryan et al. 2014; Weinberger et al. 2020; Wibking & Krumholz 2022), which we will consider implementing in the future.

##### 4.1. Domain decomposition

A 2D/3D block-structured computational domain can be mapped to a 1D list by a space-filling curve. The 1D list can then be subdivided and distributed to different memory/cores in a distributed computing system. Popular space-filling curves include the Z-order filling curve that has been adopted by *AMRVAC* and *Athena++* or the Hilbert filling curve<sup>4</sup> that is recently implemented in *Kratos* (Wang 2025) and is also adopted by *Guangqi*. Figure 3 illustrates the difference between the two space-filling curves on the same computational domain. Each color denotes a sub-domain. We can see that the Z-order curve may generate disconnected sub-domains, increase the surface-to-volume ratio, and require more communication between sub-domains. This is because when a 2D/3D domain is mapped to 1D, the blocks that are close in 2D/3D are not necessarily close in 1D, and vice versa. In principle, reducing the communication workload could improve the parallel performance. However, in our practice, we find that the performance between the two space-filling curves is insignificant. We conjecture that *Guangqi* may not have optimized to the level that this subtle difference can clearly emerge, or the surface-to-volume ratio problem is not a severe bottle-

<sup>4</sup> Hilbert space-filling curve.

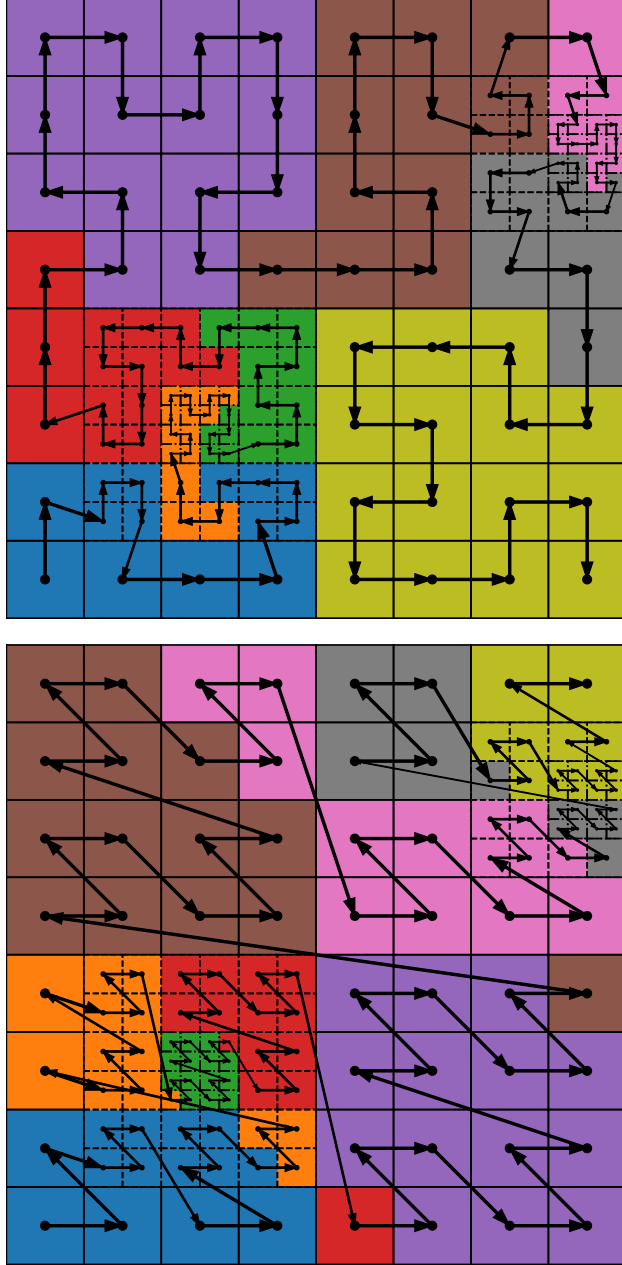


**Figure 3.** Example of domain decomposition with the same mesh refinement. The computational domain is distributed into 9 sub-domains, represented by different colors. The upper panel shows the domain decomposition of Hilbert curve, and the bottom panel shows the domain decomposition of Z-order curve.

neck in 2D problems. Thus, both the Hilbert and Z-order curves are implemented in **Guangqi**.

#### 4.2. Communications for hydrodynamic variables

Hydrodynamic solvers benefit from the uniform data structure within a block, but the cells near the blocks boundaries require prolongation, restriction and com-

munication where there is a level difference. We outline the necessary steps to communicate between the coarse and fine blocks' boundary in **Guangqi**.

1. Do cell-wise restriction on the fine block's boundary based on the conservation laws,

$$U_{i,j} = \frac{\sum_{2i-1,2j-1}^{2i,2j} U'_{i',j'}}{\sum_{2i-1,2j-1}^{2i,2j} V'_{i',j'}}, \quad (73)$$

where  $V'$  is the cell volume on the fine grid,  $U_{i,j}$  is the conserved variables on the restricted grid. Save the restricted cells for prolongation.

2. Pass the restricted cells to the guard cells of the coarse block. In the mean time, pass the original cells of the coarse blocks to the guard cells of the fine blocks.
3. Prolongate the primitive variables on the guard cells with the received data from the coarse block and the previously saved restricted local cells of fine blocks, utilizing a reconstruction method,

$$W_{2i-1,2j-1} = W'_{i,j} - \delta_x W'_{i,j} - \delta_y W'_{i,j}, \quad (74)$$

$$W_{2i-1,2j} = W'_{i,j} - \delta_x W'_{i,j} + \delta_y W'_{i,j}, \quad (75)$$

$$W_{2i,2j-1} = W'_{i,j} + \delta_x W'_{i,j} - \delta_y W'_{i,j}, \quad (76)$$

$$W_{2i,2j} = W'_{i,j} + \delta_x W'_{i,j} + \delta_y W'_{i,j}, \quad (77)$$

where  $\delta_x W'_{i,j}$  and  $\delta_y W'_{i,j}$  are the estimated differences between the prolongated variables ( $W$ ) and the original variables ( $W'$ ), utilizing the slope limited primitive variables (see Equation 26) in the  $x$  and  $y$  coordinates.

In the multilevel communication, the prolongation can be done to the primitive variables with van Leer slope limiter reconstruction without breaking the conservation law, because this prolongation is done on the guard cells of the fine grid, and we only need them to calculate the fluxes on the block boundaries. Notably, in block-wise prolongation in the SMR/AMR<sup>5</sup>, the prolongation must be done to the conservative variables with a less aggressive slope limiter, such as the minmod, to satisfy conservation laws and maintain numerical stability (Stone et al. 2020).

After the calculation of the fluxes at the interfaces, we also need to do flux correction on the coarse cells to satisfy the conservation law. The flux correction step in 2D is

$$F_{\text{coarse},j} = \frac{F_{\text{fine},2j-1} \mathcal{A}_{\text{fine},2j-1} + F_{\text{fine},2j} \mathcal{A}_{\text{fine},2j}}{\mathcal{A}_{\text{fine},2j-1} + \mathcal{A}_{\text{fine},2j}}, \quad (78)$$

<sup>5</sup> Sometimes we need to restart simulations and add refinements to specific regions.

where  $F$  is defined in Equation 21 and  $\mathcal{A}$  is the interface area. Passive scalars follow the same communication pattern as the hydrodynamic variables. The communication between the same level blocks are based on MPI derived datatypes and do not require flux correction.

### 4.3. Communications for radiation variables

As detailed in Section 3.2.2, the monolithic matrix is assembled by interpolating cell-centered quantities ( $E_r$  and  $\kappa_R \rho$ ) to determine the interface-centered variables ( $E_r$ ,  $\kappa_R \rho$ ,  $\nabla E_r$ , and  $D$ ). During the interpolation stage, the precise spatial coordinates of the neighboring cell centers (e.g., C2, C3, and C6) are required to compute the interface values at I1 and I2.

Consequently, the solver only requires a precomputation of neighboring cell locations based on the underlying grid hierarchy. By explicitly accounting for these interface interactions within the global matrix, the implicit solver maintains flux consistency across refinement levels without requiring standard prolongation or restriction operators.

## 5. NUMERICAL TESTS

In this section, we test the capability of our code in solving the general EoS hydrodynamics, radiation transport, and radiation-hydrodynamics. We also test the functionality of SMR/AMR, and the spherical coordinate system.

### 5.1. Radiation-matter coupling (0D) tests

#### 5.1.1. Radiation and perfect gas coupling

We start by examining the energy coupling between radiation and a perfect gas. Following Turner & Stone (2001) and Kolb et al. (2013), we set up a 1D domain with a constant and uniform radiation energy density  $E_r = 10^{12} \text{ erg}\cdot\text{cm}^{-3}$  and 256 cells in the Cartesian geometry. Therefore, the rank of the linear system is 512. The gas internal energy  $e_g$  should evolve according to,

$$\frac{\partial e_g}{\partial t} = -\kappa_P \rho c (a_R T_g^4 - E_r) \quad (79)$$

For this test, we choose the same parameters as the ones in Kolb et al. (2013), i.e.,  $\rho = 10^{-7} \text{ g}\cdot\text{cm}^{-3}$ ,  $v = 0$ ,  $\kappa_P = 0.4 \text{ cm}^2\cdot\text{g}^{-1}$ , and  $e_g = (3\rho k_b T_g) / (2\mu m_H)$ , with  $\mu = 0.6$  and  $m_H$  being the mean atomic weight and the mass of a hydrogen atom. To examine the accuracy of the heating and cooling processes of the gas, three initial gas conditions are chosen, they are  $e_g = [10^2, 10^6, 10^{10}] \text{ erg}\cdot\text{cm}^{-3}$ . Equation 79 can be integrated numerically by the ode45 function in Matlab. We set the initial timestep  $dt = 10^{-20} \text{ s}$  and increase the timestep by 1% after each step. The relative error is set  $\epsilon_r = 10^{-6}$ . The

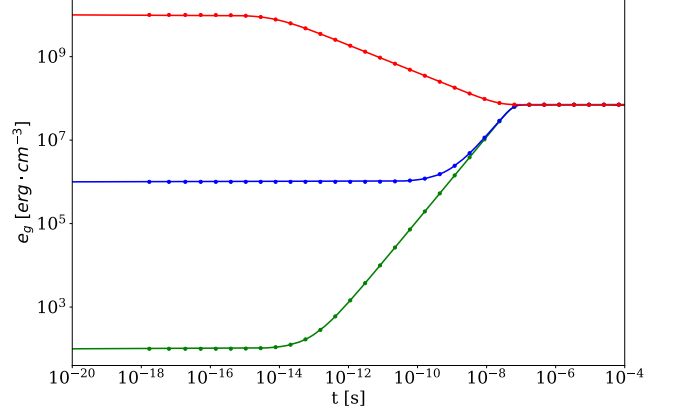


**Figure 4.** The temporal change of  $e_g$  in the radiation and perfect gas coupling tests with three different initial gas conditions.

| type    | $T_{\text{rad}}$<br>(K) | $T_g$<br>(K) | $\kappa_P$<br>( $\text{cm}^2\cdot\text{g}^{-1}$ ) | $\rho$<br>( $\text{g}\cdot\text{cm}^{-3}$ ) | $\epsilon_r$ |
|---------|-------------------------|--------------|---|---|--------------|
| heating | $10^4$                  | 4000         | 0.4   | $10^{-12}$                                  | $10^{-10}$   |
| cooling | 4000                    | $10^4$       | 0.4   | $10^{-12}$                                  | $10^{-10}$   |

**Table 1.** From the left to the right: test type; fixed radiation temperature; initial gas temperature; Planck mean opacity of the gas; density of the gas; relative error in the iterative solver.

solid lines in Figure 4 are the solution from the ode45 and the dots are the numerical solutions of **Guangqi**. The results clearly show excellent agreement between the two groups of solutions.

#### 5.1.2. Radiation and hydrogen gas coupling

Next, we test the coupling between radiation and matter that has a complex EoS. The design of the test is very similar to the test in Section 5.1.1. We solve Equation 79 and assume that the gas consists of  $\text{H}_2$ ,  $\text{H}$ ,  $\text{H}^+$ , and  $\text{e}^-$  and all the species are in LTE. A description of the EoS can be found in Chen et al. (2019). Note that  $e_g(\rho, T)$  is now a nonlinear equation of  $\rho$  and  $T$  (Figure 1). We linearize the equation and obtain,

$$C_V \frac{\partial T_g}{\partial t} = -\kappa_P \rho c (a_R T_g^4 - E_r) \quad (80)$$

where  $C_V = de_g/dT_g$  is the heat capacity of the gas. Here, we use a background radiation at constant temperature to heat/cool pure hydrogen gas that will ionize/recombine. The physical conditions of the heating/cooling test are listed in Table 1. We set the total time of integration to be  $\Delta t = 1000 \text{ s}$ .

In Section 3.2.1, we proposed to integrate Equation 80 with an increasing time-step. Figure 5 shows the evolution of the  $T_g$  with different  $q_t$  and  $n_{\text{sub}}$ . The upper

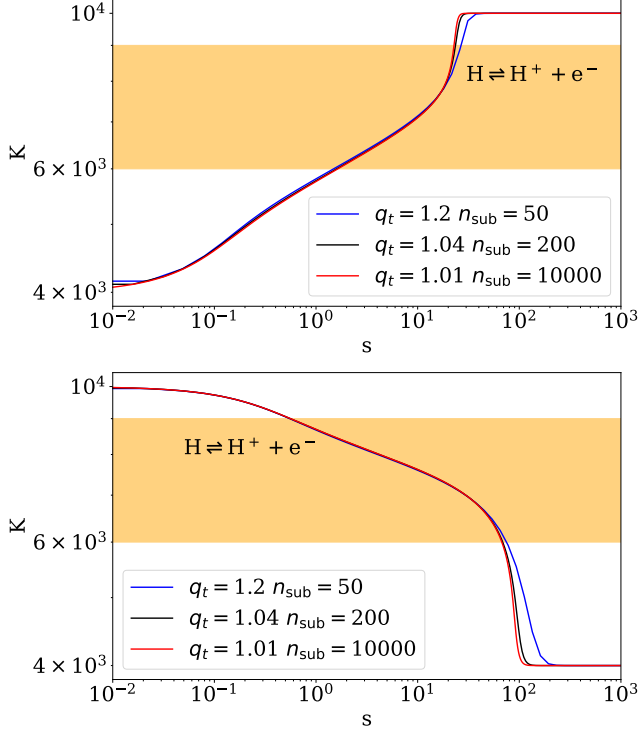


**Figure 5.** Temporal evolution of  $T_g$ . Top panel: hydrogen gas heating test; bottom panel: hydrogen gas cooling test. The radiation temperature is held constant at  $10^4$ K and 4000K for the heating/cooling test. The initial gas temperature is 4000K and  $10^4$ K for the heating/cooling test.

and bottom panels show the results of the heating and cooling tests, respectively. We can see that a combination of  $q_t = 1.2$  and  $n_{\text{sub}} = 50$  combination already gives reasonable results. In practice, the choice of  $q_t$  and  $n_{\text{sub}}$  also depend on the  $\kappa_P$  and  $\Delta t$  and can be problem dependent.

## 5.2. 1D tests

### 5.2.1. AMR with a second order general EoS HLLC Riemann solver

Here we examine the accuracy of the MUSCL scheme general EoS HLLC Riemann solver when combined with the AMR technique for the first time. We use the exact and the approximate Riemann solvers described in Chen et al. (2019).

We setup a Sod shock-tube test to examine the hydrodynamic solver. The Sod shock-tube test has a left initial state  $[\rho, v, p, T] = [10^{-11} \text{ g}\cdot\text{cm}^{-3}, 0 \text{ cm}\cdot\text{s}^{-1}, 2.4753 \times 10^1 \text{ dyn/cm}^2, 15000 \text{ K}]$ , where the gas is fully ionized. The right initial state is given by  $[\rho, v, p, T] = [10^{-12} \text{ g}\cdot\text{cm}^{-3}, 0 \text{ cm}\cdot\text{s}^{-1}, 4.1256 \times 10^{-2} \text{ dyn/cm}^2, 1000 \text{ K}]$ , where the gas is fully molecular. The CFL number is 0.9 and the simulation time is  $1.5 \times 10^{-7}$  s. The computational domain is  $[-0.5, 0.5]$  cm and  $x = 0$  separates

the left and right states. Figure 6 shows the density, velocity, pressure, and temperature profiles calculated by Guangqi and the exact solution from Chen et al. (2019). The base resolution has  $n_x = 256$  grid cells. The red hollow circles show results obtained from the base resolution, while the blue dots correspond to results with 4 levels of AMR. The refinement criterion of this test is

$$\frac{2|\rho_{i+1} - \rho_{i-1}|}{\rho_i} \geq 0.02, \quad (81)$$

which is mostly concentrated around the shock.

We first notice that beyond the shock region, the results with and without AMR both agree very well with the exact solution, including in the rarefaction wave, testifying the accuracy of our numerical scheme in general. The shock front and contact discontinuity are not properly resolved in uniform grid, but are well captured when AMR is enabled. Therefore, the AMR technique improves both accuracy and efficiency.

### 5.2.2. Dynamical radiative diffusion

In an extremely opaque environment, e.g., deep inside a star, radiation diffusion may be less efficient in transporting energy than advection. This situation, known as radiation trapping, occurs when the diffusion timescale is much longer than the advection timescale. Here, we test the coupling between the advection and diffusion parts of the radiation hydrodynamic solver of Guangqi, by solving a 1D problem with background fluid motion and radiative diffusion while turning off radiation-matter coupling (Jiang 2021). In the absence of the background fluid motion, the test will reduce to the normal diffusion problem (Commerçon et al. 2011; Kolb et al. 2013). The computational domain is  $[-2, 14]$  cm with  $N = 1024$ . We set uniform fluid conditions with  $v = 1.8 \text{ km}\cdot\text{s}^{-1}$ ,  $T_g = 0.1 \text{ K}$ , and its opacities are  $\rho\kappa_R = 10^7 \text{ cm}^{-1}$ , and  $\kappa_P = 0$ . The density of the fluid does not matter here because the fluid and the radiation are not coupled ( $\kappa_P = 0$ ). We run the simulation for  $t = 6.2 \times 10^{-5}$  s and set the CFL number to be 1 and  $\epsilon_r = 10^{-8}$ .

We set the initial condition for radiation energy density to be,

$$E_r = \begin{cases} E_0/(2\Delta x), & |\text{center}(x)| < \Delta x \\ 1, & \text{elsewhere} \end{cases} \quad (82)$$

where  $\text{center}(\cdot)$  is a function that returns the cell center's coordinate, i.e., the central two cells neighboring  $x = 0$  satisfy the first condition. The total energy of the central energy packet is set to  $E_0 = 2 \times 10^5$  erg. Both the left and right radiation boundary conditions

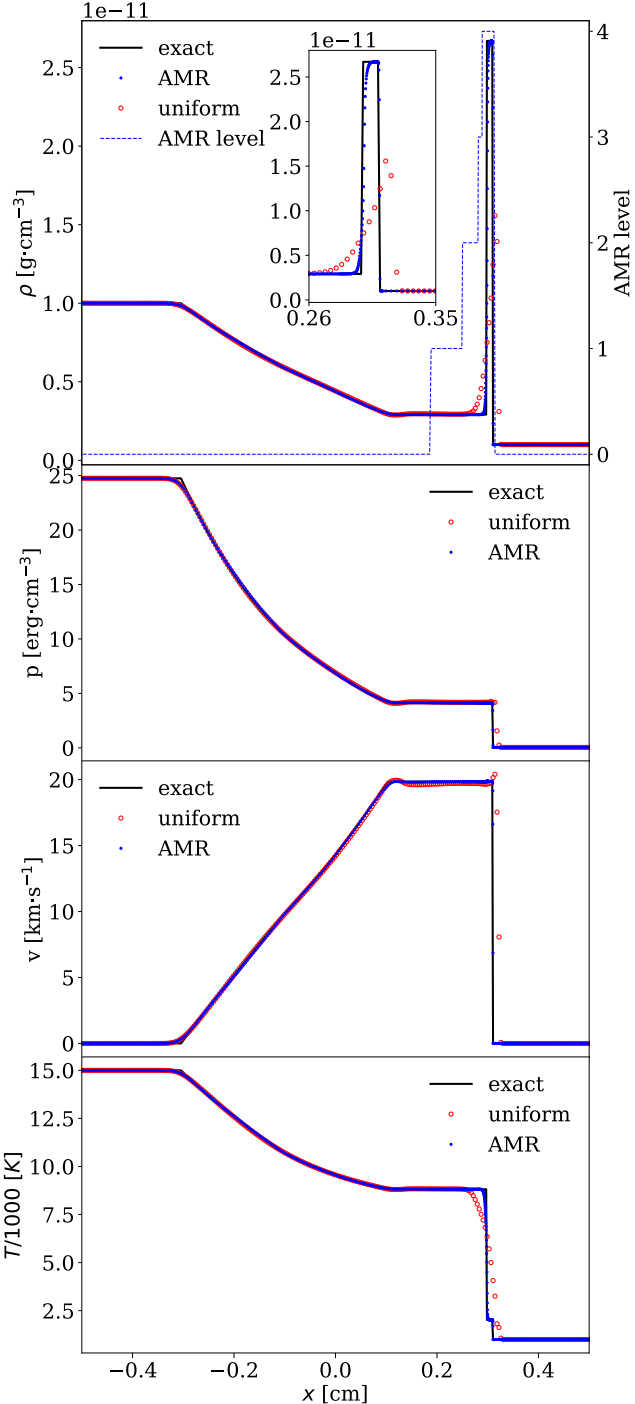


**Figure 6.** A Sod shock-tube test - with stationary high density and temperature gas on the left and stationary low density and temperature gas on the right - to examine the AMR function with the pure hydrogen EoS. From the top to the bottom, they are the density, pressure, velocity, and temperature profiles. The exact solution is in black solid lines. The blue/red dots show the approximate solution with/without AMR. The AMR level is shown on the secondary  $y$  axis with a blue dashed line in the top panel.

are zero-gradient, i.e.,  $\partial E_r / \partial r = 0$ . The fluid boundary condition is fixed at  $v = 1.8 \text{ km}\cdot\text{s}^{-1}$  and  $T_g = 0.1 \text{ K}$ .

It is straightforward to obtain the analytic solution of  $E_r$  as

$$E_a(x, t) = 1 + \frac{E_0}{\sqrt{4D\pi t}} \exp\left\{-\frac{(x-vt)^2}{4Dt}\right\}, \quad (83)$$

where  $D = c/(3\rho\kappa_R)$ . Over the duration of the test, we can calculate the characteristic diffusion length  $l_{\text{diff}} = \sqrt{4Dt} \approx 0.498 \text{ cm}$ , which is much shorter than the hydrodynamical length  $l_{\text{dyn}} = vt = 11.16 \text{ cm}$ .

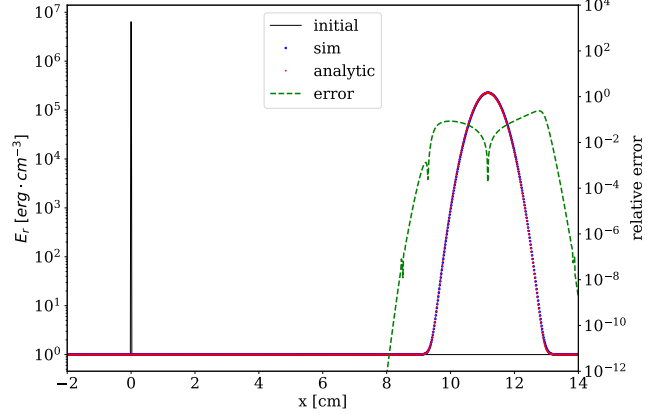


**Figure 7.** Dynamical diffusion test result at  $t = 6.2 \times 10^{-5} \text{ s}$ . Black line: the initial condition. Red and blue dots: the analytic solution and the simulated result respectively. Green dashed line: the relative error.

Figure 7 shows the initial condition, analytic solution, numerical solution, and relative error, defined as

$$\text{relative error} = \frac{|E_a - E_r|}{E_a}, \quad (84)$$

where  $E_r$  is the numerical solution. As we can see, the energy packet diffuses and advects well follows the analytical solution, and the error is kept to be relatively small. Note that in this test, advection is much more significant than diffusion given  $l_{\text{diff}} < l_{\text{dyn}}$ .

### 5.2.3. Radiative shocks with a perfect gas EoS

In this subsection, we test the full radiation hydrodynamic solver by studying radiative shocks. We follow the numerical setup of Enzman (1994) to construct the sub-critical and supercritical radiative shocks. The same setup has been adopted by Commerçon et al. (2011); Kolb et al. (2013); Colombo et al. (2019).

The physical picture of these simulations is that the gas runs into a hard and non-conducting wall and radiates away its energy in the shock. Our computational domain is  $[0, 7 \times 10^{10}] \text{ cm}$  with a base resolution of

$N = 256$ . One difference in this work is that we apply 3 levels of SMR that can cover the shock throughout the whole simulation. Therefore, the effective resolution is still 2048, which was adopted by all the aforementioned works. The gas has a uniform density of  $\rho = 7.78 \times 10^{-10}$  g·cm $^{-3}$  and a temperature  $T_g = 10$ K. The initial gas velocity is  $v_g = -6$  km·s $^{-1}$  and  $v_g = -20$  km·s $^{-1}$  for the sub-critical and super-critical radiative shock tests, and we sample the results at  $t = 38000$  s and  $t = 7500$  s, respectively. The gas is a  $\gamma$ -law gas with  $\gamma = 1.4$  and  $\mu = 1$ . We adopt constant photon mean free paths with  $\rho\kappa_R = \rho\kappa_P = 3.1 \times 10^{-10}$  cm $^{-1}$  (implying that the opacity  $\kappa_P$  and  $\kappa_R$  are set to be inversely proportional to density). The initial radiation energy density is  $E_r = a_R T_g^4$ . The CFL number is 0.4 and the relative error tolerance of the matrix solver is set to  $\epsilon_r = 10^{-5}$ . The left boundary is reflective for the fluid variables and zero-gradient for radiation. The right fluid boundary is fixed and the right radiation boundary is also zero-gradient. The fixed right fluid boundary has the same state as the corresponding initial state of the fluid.

Figure 8 shows the profiles of  $T_g$  and  $T_{\text{rad}}$  of the sub-critical and super-critical shocks. In the case of the sub-critical radiative shock,  $T_{\text{rad}} > T_g$  in the pre-shock region and  $T_g > T_{\text{rad}}$  in the post-shock region, indicating that the shock strength is not strong enough to preheat the upstream, and the shocked gas carries excess energy to the downstream. Three characteristic temperatures can be estimated analytically, which are the final equilibrium post-shock temperature (Mihalas & Mihalas 1984; Enzman 1994),

$$T_2 \approx \frac{2(\gamma - 1)v_g^2}{R_G(\gamma + 1)^2}, \quad (85)$$

the temperature immediately ahead of the shock front (Mihalas & Mihalas 1984),

$$T_- \approx \frac{\gamma - 1}{\rho v R_G} \frac{2\sigma_{\text{sb}} T_2^4}{\sqrt{3}}, \quad (86)$$

and the temperature immediately behind the shock front (Mihalas & Mihalas 1984),

$$T_+ \approx T_2 + \frac{3 - \gamma}{\gamma + 1} T_-, \quad (87)$$

where  $R_G = k_b/\mu m_H$ . Table 2 lists the analytically estimated temperature and the numerical results of three works. Our results are in agreement with the analytic estimations.

In the case of super-critical shock, we have  $T_{\text{rad}} = T_g$  in the pre-shock and post-shock region, indicating that the shock is strong enough to preheat the upstream and

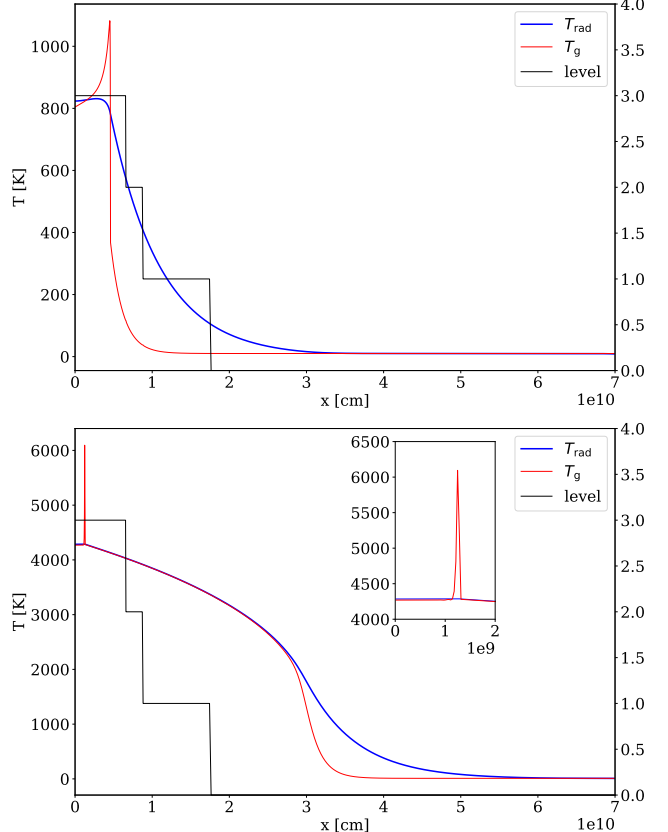


**Figure 8.** Top panel: sub-critical shock test with 3 levels of SMR applied to  $[0, 4 \times 10^9]$  cm. Bottom panel: supercritical shock test with 3 levels of SMR applied to  $[0, 4 \times 10^9]$  cm, a zoom-in plot focuses on the Zel'dovich spike. Red line: the gas temperature. Blue dots: the radiation temperature. Black solid line: the SMR level.

cools down to the equilibrium temperature in a very short distance in the downstream. The very short distance of cooling is the Zel'dovich spike.

#### 5.2.4. Radiative shocks with the hydrogen EoS

This test represents the first comprehensive numerical benchmark that integrates radiative transfer, complex EoS physics, and hydrodynamics. The setup is fundamentally similar to the supercritical shock test described in Section 5.2.3; however, in this configuration, the shock front preheats the upstream material sufficiently to trigger hydrogen ionization and dissociation. We highlight the specific modifications to the benchmark setup below:

1. To ensure the shock is capable of preheating the upstream gas to an ionized state, the gas velocity is set to  $v_g = -70$  km s $^{-1}$ . The simulation is evolved until  $t = 2500$  s.

| Temp  | Analytic         | This work | Kolb et al. (2013) | Colombo et al. (2019) |
|-------|------------------|-----------|--------------------|-----------------------|
| $T_2$ | $\approx 865$ K  | 816.7 K   | 816.6 K            | 817 K                 |
| $T_-$ | $\approx 315$ K  | 321.7 K   | 331.9 K            | 332 K                 |
| $T_+$ | $\approx 1075$ K | 1068.1 K  | 1147.1 K           | 1151 K                |

**Table 2.** Comparison of the temperature at different regions of the shock between analytical estimates and numerical results in the sub-critical radiative shock test (see Section 5.2.3). The second column is the analytic estimates. Numerical results are obtained from this work and other literature is shown in the next three columns.

2. The upstream progenitor gas is initialized in a purely molecular state.
3. For the radiation field at the right boundary, we adopt the Milne boundary condition (see Chapter 11 of Castor 2004):

$$E_r = -\frac{1}{3/2\rho\kappa_R} \frac{\partial E_r}{\partial x}, \quad (88)$$

which physically represents a blackbody absorber at the outer boundary.

4. We set  $\epsilon_r = 10^{-8}$ .

We employ the hydrogen EoS and the analytical EoS solver as described in Chen et al. (2019), which assumes chemical equilibrium among  $\text{H}_2$ ,  $\text{H}$ ,  $\text{H}^+$ , and  $e^-$ . To ensure a converged solution for the radiation-thermodynamic subsystem, we implement sub-cycling with a stretching factor of  $q_t = 1.4$ . We tested various sub-cycle counts,  $n_{\text{sub}} = \{1, 5, 6\}$ , and found that the results for  $n_{\text{sub}} = 5$  and  $n_{\text{sub}} = 6$  are nearly identical, indicating convergence.

Figure 9 shows the results of the radiative shock with a hydrogen EoS. The solid lines are the converged solutions, and for comparison, we show the solution of  $n_{\text{sub}} = 1$  in dashed lines. The top panel shows the mass fraction of different hydrogen species, defined as,

$$\chi_s = \frac{n_s m_s}{\rho}, \quad (89)$$

where  $s$  represents any species. The overall temperature profile is similar to the super-critical shock simulation of the  $\gamma$ -law gas, in which  $T_g = T_{\text{rad}}$  in the upstream and downstream of the shock. Due to the coupling between the radiation hydrodynamics and EoS, hydrogen is ionized at the Zel'dovich spike. From the shock to the upstream region, the ionization fraction gradually decreases as  $T_g$  drops. Consequently,  $\chi_{\text{H}}$  increases. In the far upstream,  $\chi_{\text{H}}$  drops rapidly between  $[4 \times 10^9, 5 \times 10^9] \text{ cm}$  because  $\text{H}_2$  is not dissociated as  $T_g$  drops. In the middle panel,  $T_g$  and  $T_{\text{rad}}$  profiles are similar to Fig 8 except that there is an additional kink in  $T_g$  due to the hydrogen dissociation. In comparison, the unresolved solution ( $n_{\text{sub}} = 1$ ) overestimates the shock

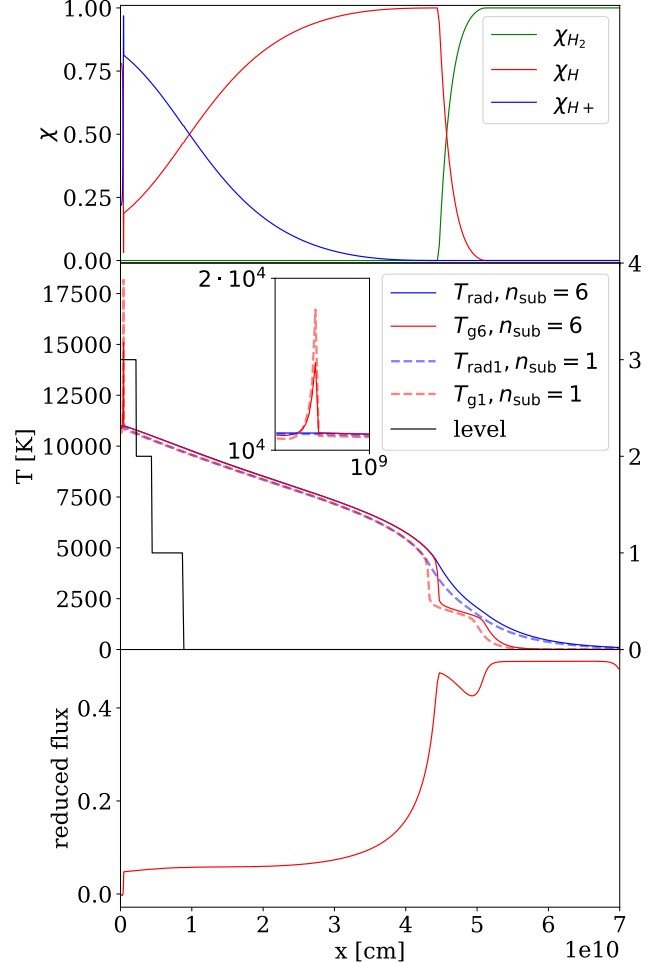


**Figure 9.** Top panel: the mass fraction of hydrogen species. Middle panel:  $T_g$  and  $T_{\text{rad}}$  of solutions with  $q_t = 1.4$  and  $n_{\text{sub}} = \{1, 6\}$ . The dashed lines are the unresolved solutions ( $n_{\text{sub}} = 1$ ) and the solid lines are the converged solutions ( $n_{\text{sub}} = 6$ ). We apply 3 levels of SMR to  $[0, 2 \times 10^9] \text{ cm}$  region. Bottom panel: reduced flux  $|\vec{F}_r|/(cE_r)$ .

temperature. The bottom panel shows the reduced flux  $\vec{F}_r/(cE_r)$ , note that the flux is not zero at the right boundary as we allow the radiation to leave the computational domain.

A closely related application of this test is the study of accreting gas giants (Chen & Bai 2022) (in a spherical coordinate), where low-angular momentum gas may fall

directly onto the atmosphere of the gas giants. Luminous shocks may form at the top layer of their atmosphere and dissociate H<sub>2</sub> of the incoming gas.

### 5.3. 2D tests

#### 5.3.1. Kelvin-Helmholtz instability

The Kelvin-Helmholtz instability (KHI) test is a standard hydrodynamic test in 2D. We follow [Stone et al. \(2020\)](#); [Wibking & Krumholz \(2022\)](#) to set up the test, where we turn off radiation transport and use Van Leer slope limiter. The boundary is periodic in both  $x$  and  $y$  directions. The computational domain is  $[-0.5, 0.5] \times [-0.5, 0.5]$ . The initial condition of the simulation is

$$\rho = 1.5 - 0.5 \tanh\left(\frac{|y| - 0.25}{L_1}\right), \quad (90)$$

$$v_x = 0.5 \tanh\left(\frac{|y| - 0.25}{L_1}\right), \quad (91)$$

$$v_y = A \cos(4\pi x) \exp\left[-\frac{(|y| - 0.25)}{L_2^2}\right]. \quad (92)$$

with the shearing layer thickness  $L_1 = 0.01$ ,  $L_2 = 0.2$ , and perturbation amplitude  $A = 0.01$ . The initial pressure is uniform with  $p = 2.5$  and we adopt an adiabatic index  $\gamma = 1.4$ . We run the simulation with both uniform high resolution and AMR. The uniform high resolution is  $2048 \times 2048$ , and the base level of the AMR simulation has a resolution of  $256 \times 256$  with 3 levels of mesh refinement, thus the effective highest resolution is also  $2048 \times 2048$ . The refinement criteria are

$$(\Delta x \|\nabla v_x\|)/v_x > 0.01, \quad \text{or} \quad (93)$$

$$(\Delta x \|\nabla v_y\|)/v_y > 0.01, \quad (94)$$

and the derefinement criteria are,

$$(\Delta x \|\nabla v_x\|)/v_x < 0.005, \quad \text{and} \quad (95)$$

$$(\Delta x \|\nabla v_y\|)/v_y < 0.005, \quad (96)$$

We choose the CFL number to be 0.4 and stop the simulation at  $t = 1.2$ . The simulations are run on an AMD EPYC 7763 CPU with 32 cores.

We present the results in Figure 10. The density structure on the left panel is similar to the results from other works. The middle panel shows that the vortices are resolved by high resolution while the interior of the streams does not require high resolution. The domain decomposition into 16 cores is according to the Hilbert curve, and each sub-domain is connected. We compare the AMR simulation to uniform high resolution simulation by plotting their density profile at  $t = 1.2$  and  $y = 0.25$ , where the density gradient is the steepest. On

this horizontal line, the AMR simulation has low resolution and high resolution regions but the difference between the red line (fixed high resolution) and black dots is indistinguishable. Quantitatively, we interpolate the AMR density on the uniform grid to calculate their relative difference by,

$$\delta\rho_{\text{khi}} = (\rho_{\text{AMR}} - \rho_{\text{uniform}})/\rho_{\text{uniform}}. \quad (97)$$

The relative difference is within 0.4%, similar to the results in other works.

#### 5.3.2. Performance of PSAMA

To evaluate the robustness and performance of the PSAMA scheme (Section 3.1.2), we utilize an isolated, inviscid, and locally isothermal hydrostatic thin-disk model. In spherical polar coordinates, the governing Euler equations for this hydrostatic configuration are given by:

$$\frac{v_\phi^2}{r} = g + \frac{1}{\rho} \frac{\partial p}{\partial r}, \quad (98)$$

$$v_\phi^2 \cot\theta = \frac{1}{\rho} \frac{\partial p}{\partial \theta}, \quad (99)$$

where  $g = GM_s/r^2$  is the central gravity,  $p$  is the ideal gas pressure. We can obtain  $v_\phi$  from Equation 98,

$$v_\phi^2 = rg + T \left( \frac{\partial \ln T}{\partial \ln r} + \frac{\partial \ln \rho}{\partial \ln r} \right). \quad (100)$$

To make it an isolated disk in a nearly vacuum circumstance, we assume  $\rho$  and  $T$  to have the following dependence on  $r$  and  $\theta$ ,

$$\rho = \rho_0 \left( \frac{r}{r_0} \right)^a \text{sig}_1(r) \text{sig}_2(r) f(\theta) \quad (101)$$

$$\text{sig}_1(r) = (1 + \exp(-d_1(r - r_{\text{in}})/r_{\text{in}}))^{-1} \quad (102)$$

$$\text{sig}_2(r) = (1 + \exp(d_2(r - r_{\text{out}})/r_{\text{out}}))^{-1} \quad (103)$$

$$T = T_0 \left( \frac{r}{r_0} \right)^b = \frac{p_0}{\rho_0} \left( \frac{r}{r_0} \right)^b, \quad (104)$$

where  $\text{sig}_1(r)$  is to create an inner cavity,  $\text{sig}_2(r)$  is to truncate the outer disk,  $r_{\text{in}}$ ,  $r_{\text{out}}$ ,  $d_1$ , and  $d_2$  controls the location of the inner cavity, truncation radius, gradient of the density slopes, respectively. In addition,  $r_0$ ,  $\rho_0$ ,  $T_0$ ,  $p_0$ ,  $a$ , and  $b$  are constants that create the power-law part of the disk profiles. Equation 100-104 characterizes an isolated hydrostatic disk. To calculate  $f(\theta)$ , we solve Equation 99,

$$\frac{v_\phi^2}{T} = \frac{\partial \ln \rho}{\partial \ln \sin \theta}. \quad (105)$$

As a result,

$$f(\theta) = (\sin \theta)^{v_\phi^2/T}. \quad (106)$$

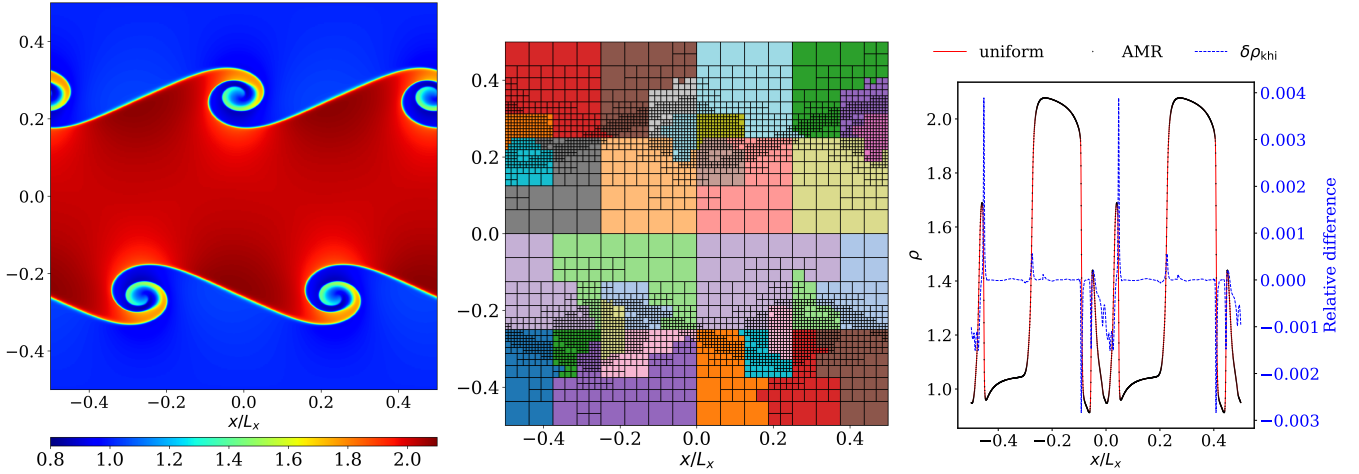


**Figure 10.** Results of the Kelvin-Helmholz instability test at  $t = 1.2$ . Left panel: the density of the AMR simulation. Middle panel: the AMR block structure and domain decomposition into 32 cores colored according “tab20” colormap periodically. Right panel: the density profile at  $y = 0.25$  and  $t = 1.2$ , the red line and black dots show the simulation results of fixed resolution ( $2048 \times 2048$ ) and AMR ( $256 \times 256$  with 3 levels of mesh refinement).

In a hydrostatic disk, the only non-zero physical variables are the azimuthal velocity  $v_\phi$ , density  $\rho$ , and temperature  $T$ , as defined by Equations 100, 101, and 104, respectively. When initialized in a steady state, the analytical profile should relax to a numerical equilibrium that remains close to the initial condition. However, Equation 106 implies that the polar regions will reach extremely low densities. To handle this numerically, we implement a density floor during initialization. A sufficiently low floor density ensures that the ambient environment approximates a vacuum, thereby minimizing its dynamical impact on the disk.

For this validation test, we adopt the following dimensionless parameters:  $M_s G = 1$ ,  $r_0 = 1$ ,  $r_{\text{in}} = 4$ ,  $r_{\text{out}} = 16$ ,  $d_1 = 15$ ,  $d_2 = 30$ ,  $\rho_0 = 1$ ,  $T_0 = 0.0022$ ,  $p_0 = 0.0022$ ,  $a = -2$ , and  $b = -1$ . Thus, the disk scale height is  $H/R = 0.047$ . We set the simulation domain to be  $r \in [1, 40]$  and  $\theta \in [0, \pi/2]$ . The resolution of the simulation is  $512 \times 128$ . The mesh is stretched (non-uniform grid) in the  $r$  coordinate with a ratio of  $q_r = 1.0058682$  ( $\Delta r_{i+1} = q_r \Delta r_i$ ,  $\Delta r_i$  is the  $i$ th cell size) so that the spacing is logarithmic and uniform in the  $\theta$  coordinate.

We set the CFL number to 0.5 and apply mirror symmetry boundary conditions at both the equator and the pole. The inner and outer radial boundaries are maintained at constant density and temperature with zero rotation:  $\rho_{\text{in}} = 10^{-6}$ ,  $\rho_{\text{out}} = 10^{-18}$ ,  $T_{\text{in}} = 0.0022$ , and  $T_{\text{out}} = 5.5 \times 10^{-5}$ . During initialization, if the density calculated by Equation 101 falls below  $\rho_{\text{out}}$ , we set  $\rho = \rho_{\text{out}}$  and the angular momentum to zero. Notably, we do not enforce a density floor during the subsequent hydrodynamic evolution, as the combination of

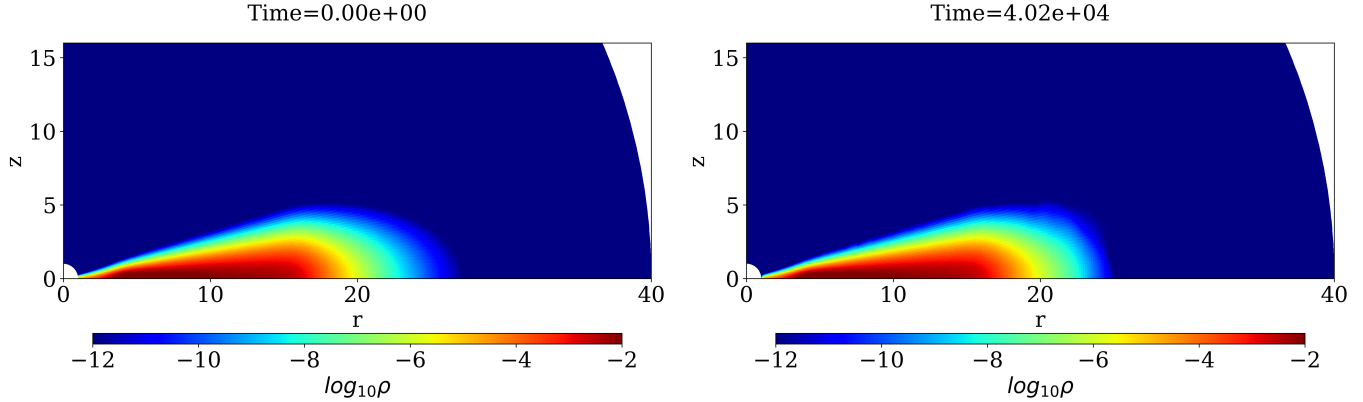
the CFL condition and the PSAMA scheme ensures density positivity. The extremely low-density ambient gas ( $\rho_{\text{out}}/\rho_0 = 10^{-18}$ ) with zero angular momentum eventually infalls from the outer boundary; however, its low inertia ensures a negligible impact on the global evolution of the disk.

We evolve the simulation for a total duration of  $t = 6,400 P_{\text{in}}$ , where  $P_{\text{in}} = 2\pi$  corresponds to the Keplerian orbital period at the reference radius  $r_0$ . This timespan is equivalent to 800 orbital periods at the inner edge ( $r_{\text{in}}$ ) of the isolated disk, providing a rigorous test of the code’s ability to maintain hydrostatic equilibrium over secular timescales. Figure 11 shows the initial density condition and the final density state of the disk. The two profiles remain remarkably similar, with the only discernible differences occurring in the extremely low-density regions. These minor deviations are attributed to the continuous infall of ambient gas from the outer boundary. Furthermore, we evaluate the impact of the source term integration accuracy by comparing simulations using the first- and second-order integrators described in Appendix C. The relative differences between these two approaches are illustrated in Figure 12, defined as:

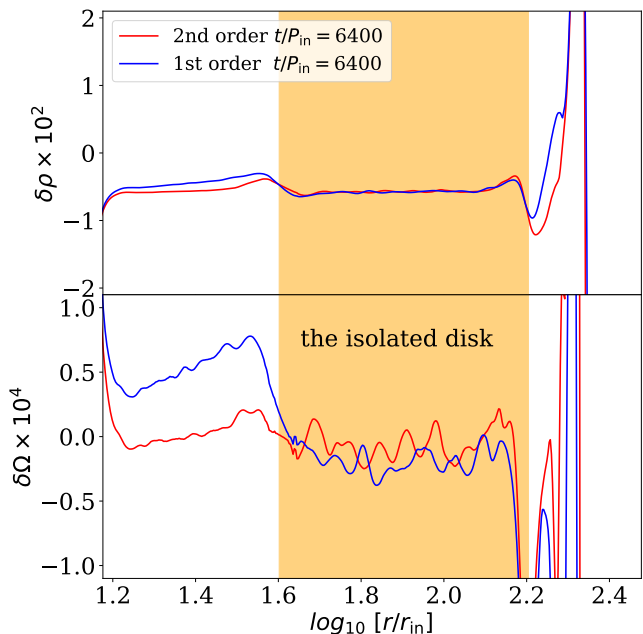
$$\delta\rho = \frac{\rho_{\text{final}} - \rho_{\text{init}}}{\rho_{\text{init}}}, \quad (107)$$

$$\delta\Omega = \frac{\Omega_{\text{final}} - \Omega_{\text{init}}}{\Omega_{\text{init}}}, \quad (108)$$

of the midplane profiles at  $t = 6400 P_{\text{in}}$ , where “init” in the subscript means the initial state. We can see that both the first and second order source term integrators can maintain the isolated disk well. The second order source term integrator has smaller variation in  $\Omega$ .



**Figure 11.** The density of the main body of the disk at different times. Left: the initial density condition of the isolated disk. Right: the density at  $t = 6400P_{\text{in}}$ .



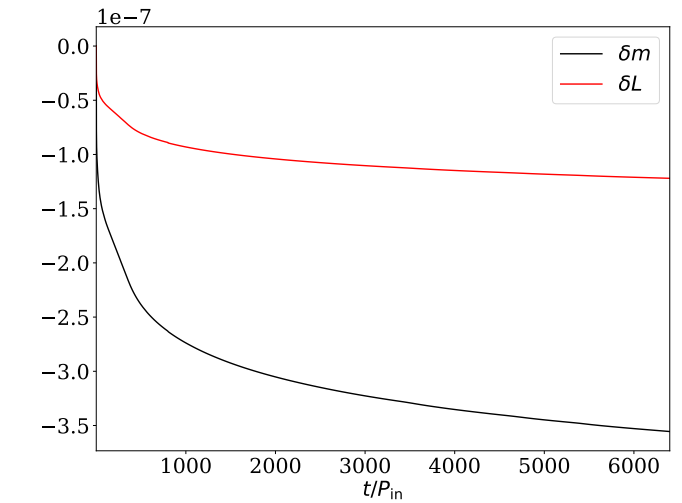
**Figure 12.** The midplane profiles of the isolated disk, using first order and second order source terms (Appendix C) at  $t = 6400P_{\text{in}}$ , including the steady state solutions in dashed black lines. The orange region is the main body of the isolated disk.

Figure 13 illustrates the relative change in the total mass and angular momentum of the disk, defined as:

$$\delta m = \frac{m_{\text{disk}}}{m_{\text{disk,init}}} - 1, \quad (109)$$

$$\delta L = \frac{L_{\text{disk}}}{L_{\text{disk,init}}} - 1, \quad (110)$$

where  $m_{\text{disk}}$  and  $L_{\text{disk}}$  represent the integrated mass and angular momentum within the computational domain. The relative fluctuations in these quantities are remarkably small, on the order of  $10^{-7}$ . We observe a relatively rapid adjustment during the initial orbits as the analytical steady state relaxes into a numerical equilibrium and



**Figure 13.** The relative change in mass and angular momentum in the computational domain with the second order scheme (Appendix C).

a small fraction of the gas exits through the inner boundary. Following this transient phase, the rate of change becomes extremely slow but remains non-zero. This minor evolution can be attributed to two primary factors: (1) the presence of inherent numerical viscosity which facilitates a slow accretion process, and (2) the continuous inflow of zero-angular-momentum ambient gas from the outer boundary, which eventually traverses the inner boundary and carries away a negligible fraction of the disk mass. Given that the relative change is less than  $10^{-10}$  per orbit, the precision of the PSAMA scheme is more than sufficient for high-fidelity simulations of long-term disk evolution.

For benchmarking purposes, we performed the same isolated disk test using the **Athena++** framework. We found that maintaining numerical stability in **Athena++** required a relatively high density floor,  $\rho_{\text{floor}}/\rho_0 \sim 10^{-10}$ , to ensure the calculation proceeded without fail-

ure<sup>6</sup>. Reducing the floor density further resulted in either prohibitively small timesteps or code crashes.

Preliminary investigation suggests that the instability is localized in regions of steep density gradients. This behavior likely stems from the fact that while the Riemann fluxes are modified in the  $\phi$ -momentum (angular momentum) component to ensure conservation, the energy flux is not adjusted commensurately (see Appendix A). This lack of synchronization can lead to unphysical or negative temperatures within a half-timestep. While a higher  $\rho_{\text{floor}}$  can circumvent these numerical artifacts, it introduces an ambient medium with sufficient inertia to perturb the disk, preventing it from maintaining its initial state over many secular timescales.

#### 5.4. Scalings and performance

##### 5.4.1. The weak scaling of pure hydrodynamics

We evaluate the parallel scaling of **Guangqi** using the KHI simulation described in Section 5.3.1, employing SMR grid configurations. These scaling tests were performed on a Sugon cluster; each node consists of 2 CPUs with 32 cores and a base clock frequency of 2.5 GHz. Our setup uses a base resolution of  $512 \times 512$  with a block size of  $32 \times 32$ , which represents a typical configuration for production runs. The two SMR levels are centered on the intervals  $y \in [0.245, 0.255]$  and  $y \in [-0.255, -0.245]$ . To assess weak scaling, we extend the domain in the  $x$ -direction accordingly. The tests were executed across  $[1, 2, 4, 8, 16]$  nodes using 52 cores per node, such that each core processes 16 blocks. The upper panel of Figure 14 illustrates the weak scaling efficiency (normalized to a single node) and the corresponding update speed. We find that the weak scaling efficiency remains above 96% up to 16 nodes (832 cores), demonstrating excellent parallel performance in the hydrodynamic part of the code, sufficient for considering more challenging scaling test incorporating radiation.

##### 5.4.2. The strong scaling of radiation hydrodynamics

We utilize the supercritical shock setup described in Section 5.2.3 and extend it to a 2D domain (uniform in the  $y$ -direction) to evaluate the RHD performance of **Guangqi**. Since iterative solvers are inherently nonlinear, we assess the strong scaling of the RHD module across varying total cell counts.

The base resolution in the  $x$ -coordinate is  $n_x = 512$  over the range  $x \in [0, 7 \times 10^{10}]$ . In the  $y$ -coordinate, we test base resolutions of  $n_y = [2048, 4096, 8192]$  over corresponding ranges of  $y_{\text{max}} = [2.8 \times 10^{11}, 5.6 \times$

<sup>6</sup> In contrast, **Guangqi** does not require an enforced  $\rho_{\text{floor}}$  during the hydrodynamic update.

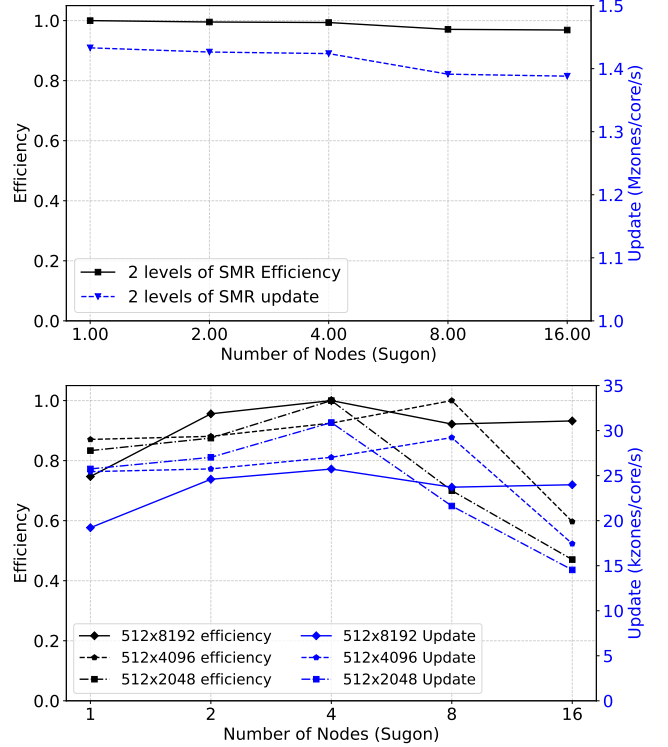


**Figure 14.** Upper panel: the weak scaling efficiency and performance ( $\text{Mzones}=10^6$  zones) of pure hydrodynamics, maintains above 96% on 16 nodes. Bottom panel: The strong scaling efficiency and performance ( $\text{kzones}=10^3$  zones) of radiation hydrodynamics of **Guangqi**.

$10^{11}, 1.12 \times 10^{12}]$ . One level of SMR is applied to the region  $x \in [0, 1.75 \times 10^{10}]$ . With a fixed block size of  $32 \times 32$ , the total number of blocks for these cases is [1792, 3584, 7168]. Strong scaling tests were conducted on  $[1, 2, 4, 8, 16]$  nodes, utilizing 56 cores per node. For these tests, we set  $\epsilon_r = 10^{-6}$  and perform a single radiation transport calculation per hydrodynamic timestep ( $n_{\text{sub}} = 1$ ).

The strong scaling efficiencies (normalized to the most efficient node count) and the update speeds are shown in the bottom panel of Figure 14. The efficiency curve exhibits non-linear behavior, which we attribute to the complexity of the iterative solvers. Our results suggest an optimal core count exists for specific problem scales; empirically, we find that a workload of approximately  $8-32 \times 10^3$  cells per core is required to maintain high performance. In practice, for instance, our target applications with 2D axisymmetric simulations often require fewer than  $10^6$  cells when utilizing SMR and non-uniform grids, making 1–4 nodes sufficient for most production runs. Notably, the RHD calculation is approximately 50–60 times more computationally expensive than pure hydrodynamics. Given that certain

regimes may require subcycling (Section 5.2.4), optimizing RHD computational efficiency remains a primary objective for future development.

## 6. SUMMARY AND DISCUSSION

In this work, we present **Guangqi**, a new two-dimensional (2D) finite-volume radiation hydrodynamics code. **Guangqi** features a general EoS framework coupled with a fully implicit radiation transport solver under the FLD approximation. It supports block-based SMR/AMR, following the architectural paradigms of codes such as **Athena++** and **Enzo**. The code supports both Cartesian and spherical-polar coordinates with non-uniform grid spacing; notably, our spherical-polar implementation is specifically designed to enhance robustness while strictly conserving angular momentum. Our primary technical highlights include:

1. General EoS Hydrodynamics: **Guangqi** solves the hydrodynamic equations using the MUSCL scheme integrated with a general EoS HLLC Riemann solver (Chen et al. 2019) (Section 3.1.1). In Section 5.2.1, we present—for the first time—the combination of AMR and the MUSCL scheme for non-ideal fluids, validating our results against exact general EoS Riemann solutions.
2. Angular Momentum Conservation: In spherical-polar coordinates, the hydrodynamic solver is architected to conserve angular momentum by ensuring compatibility between the Riemann solver and the flux divergence law (Section 3.1.2). This approach, termed the Passive Scalar Angular Momentum Algorithm (PSAMA), is validated using a specialized isolated disk test in Section 5.3.2.
3. High-Order Source Terms: To improve accuracy in astrophysical contexts, we implement second-order source terms for geometry and gravity (Appendix C). By utilizing the reconstructed slopes from the hydrodynamic solver, these terms are hard-coded into the **Guangqi** pipeline to maximize computational efficiency.
4. Multilevel Implicit Solver: In the presence of SMR/AMR, **Guangqi** solves the multilevel radiation transport and thermodynamic coupling

within a single matrix. This unified approach ensures superior energy conservation and consistency across refinement boundaries (Section 3.2.2).

With its ability to integrate realistic EoS, radiation transport, and the PSAMA formulation, **Guangqi** is well-positioned for a diverse range of applications, particularly involving accretion disks, phase transitions, and optically thick environments. Currently, as a 2D code, **Guangqi** is primarily suited for axisymmetric systems. Future extension to 3D, incorporating the PSAMA framework, will enable more realistic investigations of non-axisymmetric disk dynamics.

Finally, we note that the reliance on the FLD approximation introduces inherent limitations in transition regions between optically thin and thick regimes, as well as in highly anisotropic radiation fields. Furthermore, the computational cost of the implicit solver increases with cell number ( $N$ ) and relative error tolerances ( $\epsilon_r$ ). Our experience indicate that the solver runtime scales approximately as  $N \log N$ , though the dependence on  $\epsilon_r$  remains complex. A more exhaustive performance analysis and optimization of the implicit framework remain subjects for future research.

The authors would give special thanks to Matthew Knepley and Pierre Jolive for their help with **Petsc** code. We also thank (Alphabetic) Pinghui Huang, Hui Li, Shude Mao, Yuan-sen Ting, Kengo Tomida, Lile Wang, and Weixiao Wang for inspirational discussions. This work is supported by the National Science Foundation of China under grants No. 12103028, 12233004, 12325304, 12473030, 12342501, Tsinghua University Dushi Program and Tsinghua University Initiative Scientific Research Program No. 20233080026. Z.C thank Tsinghua Astrophysics Outstanding Fellowship, and Shuimu Tsinghua Scholar Program for financial support. The Center of High performance computing at Tsinghua University and the National Supercomputer Center in Tianjin provided the computational resources.

*Software:* Matlab (MATLAB 2018), Matplotlib (Hunter 2007), Petsc (Balay et al. 1997, 2024)

## REFERENCES

Balay, S., Gropp, W. D., McInnes, L. C., & Smith, B. F. 1997, in Modern Software Tools in Scientific Computing, ed. E. Arge, A. M. Bruaset, & H. P. Langtangen (Birkhäuser Press), 163–202

Balay, S., Abhyankar, S., Adams, M. F., et al. 2024, PETSc/TAO Users Manual, Tech. Rep. ANL-21/39 - Revision 3.22, Argonne National Laboratory, doi: [10.2172/2205494](https://doi.org/10.2172/2205494)

Batten, P., Clarke, N., Lambert, C., & Causon, D. M. 1997, SIAM Journal on Scientific Computing, 18, 1553, doi: [10.1137/S1064827593260140](https://doi.org/10.1137/S1064827593260140)

Bhandare, A., Kuiper, R., Henning, T., et al. 2018, A&A, 618, A95, doi: [10.1051/0004-6361/201832635](https://doi.org/10.1051/0004-6361/201832635)

Bloch, H., Tremblin, P., González, M., Padoleau, T., & Audit, E. 2021, A&A, 646, A123, doi: [10.1051/0004-6361/202038579](https://doi.org/10.1051/0004-6361/202038579)

Bryan, G. L., Norman, M. L., O’Shea, B. W., et al. 2014, ApJS, 211, 19, doi: [10.1088/0067-0049/211/2/19](https://doi.org/10.1088/0067-0049/211/2/19)

Castor, J. I. 2004, Radiation Hydrodynamics

Chen, Z. 2025, arXiv e-prints, arXiv:2510.14173, doi: [10.48550/arXiv.2510.14173](https://doi.org/10.48550/arXiv.2510.14173)

Chen, Z., & Bai, X. 2022, ApJL, 925, L14, doi: [10.3847/2041-8213/ac4ca9](https://doi.org/10.3847/2041-8213/ac4ca9)

Chen, Z., Coleman, M. S. B., Blackman, E. G., & Frank, A. 2019, Journal of Computational Physics, 388, 490, doi: [10.1016/j.jcp.2019.03.016](https://doi.org/10.1016/j.jcp.2019.03.016)

Chen, Z., & Ivanova, N. 2024, ApJL, 963, L35, doi: [10.3847/2041-8213/ad2a47](https://doi.org/10.3847/2041-8213/ad2a47)

Colombo, S., Ibgui, L., Orlando, S., et al. 2019, A&A, 631, A41, doi: [10.1051/0004-6361/201935991](https://doi.org/10.1051/0004-6361/201935991)

Commerçon, B., Debout, V., & Teyssier, R. 2014, A&A, 563, A11, doi: [10.1051/0004-6361/201322858](https://doi.org/10.1051/0004-6361/201322858)

Commerçon, B., Teyssier, R., Audit, E., Hennebelle, P., & Chabrier, G. 2011, A&A, 529, A35, doi: [10.1051/0004-6361/201015880](https://doi.org/10.1051/0004-6361/201015880)

Courant, R., Friedrichs, K., & Lewy, H. 1928, Mathematische Annalen, 100, 32, doi: [10.1007/BF01448839](https://doi.org/10.1007/BF01448839)

Davis, S. W., Jiang, Y.-F., Stone, J. M., & Murray, N. 2014, ApJ, 796, 107, doi: [10.1088/0004-637X/796/2/107](https://doi.org/10.1088/0004-637X/796/2/107)

Davis, S. W., Stone, J. M., & Jiang, Y.-F. 2012, ApJS, 199, 9, doi: [10.1088/0067-0049/199/1/9](https://doi.org/10.1088/0067-0049/199/1/9)

Dubroca, B., & Feugeas, J. 1999, Academie des Sciences Paris Comptes Rendus Serie Sciences Mathematiques, 329, 915, doi: [10.1016/S0764-4442\(00\)87499-6](https://doi.org/10.1016/S0764-4442(00)87499-6)

Enzman, L. 1994, ApJ, 424, 275, doi: [10.1086/173889](https://doi.org/10.1086/173889)

Fang, Q., Maeda, K., Ye, H., Moriya, T. J., & Matsumoto, T. 2025, ApJ, 978, 35, doi: [10.3847/1538-4357/ad8b19](https://doi.org/10.3847/1538-4357/ad8b19)

Fryxell, B., Olson, K., Ricker, P., et al. 2000, ApJS, 131, 273, doi: [10.1086/317361](https://doi.org/10.1086/317361)

Gnedin, N. Y., & Abel, T. 2001, NewA, 6, 437, doi: [10.1016/S1384-1076\(01\)00068-9](https://doi.org/10.1016/S1384-1076(01)00068-9)

González, M., Audit, E., & Huynh, P. 2007, A&A, 464, 429, doi: [10.1051/0004-6361:20065486](https://doi.org/10.1051/0004-6361:20065486)

Hameury, J. M. 2020, Advances in Space Research, 66, 1004, doi: [10.1016/j.asr.2019.10.022](https://doi.org/10.1016/j.asr.2019.10.022)

Howell, L. H., & Greenough, J. A. 2003, Journal of Computational Physics, 184, 53, doi: [10.1016/S0021-9991\(02\)00015-3](https://doi.org/10.1016/S0021-9991(02)00015-3)

Hunter, J. D. 2007, Computing in Science & Engineering, 9, 90, doi: [10.1109/MCSE.2007.55](https://doi.org/10.1109/MCSE.2007.55)

Ivanova, N., Justham, S., Chen, X., et al. 2013, A&A Rv, 21, 59, doi: [10.1007/s00159-013-0059-2](https://doi.org/10.1007/s00159-013-0059-2)

Jiang, Y.-F. 2021, ApJS, 253, 49, doi: [10.3847/1538-4365/abe303](https://doi.org/10.3847/1538-4365/abe303)

Jiang, Y.-F., Stone, J. M., & Davis, S. W. 2012, ApJS, 199, 14, doi: [10.1088/0067-0049/199/1/14](https://doi.org/10.1088/0067-0049/199/1/14)

Ju, W., Stone, J. M., & Zhu, Z. 2016, ApJ, 823, 81, doi: [10.3847/0004-637X/823/2/81](https://doi.org/10.3847/0004-637X/823/2/81)

—. 2017, ApJ, 841, 29, doi: [10.3847/1538-4357/aa705d](https://doi.org/10.3847/1538-4357/aa705d)

Kannan, R., Vogelsberger, M., Marinacci, F., et al. 2019, MNRAS, 485, 117, doi: [10.1093/mnras/stz287](https://doi.org/10.1093/mnras/stz287)

Käppeli, R. 2022, Living Reviews in Computational Astrophysics, 8, 2, doi: [10.1007/s41115-022-00014-6](https://doi.org/10.1007/s41115-022-00014-6)

Keppens, R., Nool, M., Tóth, G., & Goedbloed, J. P. 2003, Computer Physics Communications, 153, 317, doi: [10.1016/S0010-4655\(03\)00139-5](https://doi.org/10.1016/S0010-4655(03)00139-5)

Kley, W. 1989, A&A, 208, 98

Kolb, S. M., Stute, M., Kley, W., & Mignone, A. 2013, A&A, 559, A80, doi: [10.1051/0004-6361/201321499](https://doi.org/10.1051/0004-6361/201321499)

Larson, R. B. 1969, MNRAS, 145, 271, doi: [10.1093/mnras/145.3.271](https://doi.org/10.1093/mnras/145.3.271)

Lasota, J.-P. 2001, NewAR, 45, 449, doi: [10.1016/S1387-6473\(01\)00112-9](https://doi.org/10.1016/S1387-6473(01)00112-9)

Levermore, C. D. 1984, JQSRT, 31, 149, doi: [10.1016/0022-4073\(84\)90112-2](https://doi.org/10.1016/0022-4073(84)90112-2)

Levermore, C. D., & Pomraning, G. C. 1981, ApJ, 248, 321, doi: [10.1086/159157](https://doi.org/10.1086/159157)

Ma, J.-Z., Pakmor, R., Justham, S., & de Mink, S. E. 2025, arXiv e-prints, arXiv:2503.16627, doi: [10.48550/arXiv.2503.16627](https://doi.org/10.48550/arXiv.2503.16627)

MATLAB. 2018, 9.7.0.1190202 (R2019b) (Natick, Massachusetts: The MathWorks Inc.)

Melon Fuksman, J. D., Klahr, H., Flock, M., & Mignone, A. 2021, ApJ, 906, 78, doi: [10.3847/1538-4357/abc879](https://doi.org/10.3847/1538-4357/abc879)

Mignone, A. 2014, Journal of Computational Physics, 270, 784, doi: [10.1016/j.jcp.2014.04.001](https://doi.org/10.1016/j.jcp.2014.04.001)

Mignone, A., Bodo, G., Massaglia, S., et al. 2007, ApJS, 170, 228, doi: [10.1086/513316](https://doi.org/10.1086/513316)

Mihalas, D., & Mihalas, B. W. 1984, Foundations of radiation hydrodynamics

Minerbo, G. N. 1978, JQSRT, 20, 541, doi: [10.1016/0022-4073\(78\)90024-9](https://doi.org/10.1016/0022-4073(78)90024-9)

Moreno, M. M., Schneider, F. R. N., Röpke, F. K., et al. 2022, A&A, 667, A72, doi: [10.1051/0004-6361/202142731](https://doi.org/10.1051/0004-6361/202142731)

Popov, D. V. 1993, ApJ, 414, 712, doi: [10.1086/173117](https://doi.org/10.1086/173117)

Ramsey, J. P., & Dullemond, C. P. 2015, A&A, 574, A81, doi: [10.1051/0004-6361/201424954](https://doi.org/10.1051/0004-6361/201424954)

Saad, Y., & Schultz, M. H. 1986, SIAM Journal on scientific and statistical computing, 7, 856

Skinner, M. A., & Ostriker, E. C. 2010, ApJS, 188, 290, doi: [10.1088/0067-0049/188/1/290](https://doi.org/10.1088/0067-0049/188/1/290)

—. 2013, ApJS, 206, 21, doi: [10.1088/0067-0049/206/2/21](https://doi.org/10.1088/0067-0049/206/2/21)

Smith, N. 2017, in Handbook of Supernovae, ed. A. W. Alsabti & P. Murdin, 403, doi: [10.1007/978-3-319-21846-5\\_38](https://doi.org/10.1007/978-3-319-21846-5_38)

Stone, J. M., Tomida, K., White, C. J., & Felker, K. G. 2020, ApJS, 249, 4, doi: [10.3847/1538-4365/ab929b](https://doi.org/10.3847/1538-4365/ab929b)

Toro, E. F. 2013, Riemann solvers and numerical methods for fluid dynamics: a practical introduction (Springer Science & Business Media)

Turner, N. J., & Stone, J. M. 2001, ApJS, 135, 95, doi: [10.1086/321779](https://doi.org/10.1086/321779)

Tylenda, R., Hajduk, M., Kamiński, T., et al. 2011, A&A, 528, A114, doi: [10.1051/0004-6361/201016221](https://doi.org/10.1051/0004-6361/201016221)

van Leer, B. 1974, Journal of Computational Physics, 14, 361, doi: [10.1016/0021-9991\(74\)90019-9](https://doi.org/10.1016/0021-9991(74)90019-9)

Vetter, M., Röpke, F. K., Schneider, F. R. N., et al. 2024, A&A, 691, A244, doi: [10.1051/0004-6361/202451579](https://doi.org/10.1051/0004-6361/202451579)

Wang, L. 2025, arXiv e-prints, arXiv:2501.02317, doi: [10.48550/arXiv.2501.02317](https://doi.org/10.48550/arXiv.2501.02317)

Weinberger, R., Springel, V., & Pakmor, R. 2020, ApJS, 248, 32, doi: [10.3847/1538-4365/ab908c](https://doi.org/10.3847/1538-4365/ab908c)

Wibking, B. D., & Krumholz, M. R. 2022, MNRAS, 512, 1430, doi: [10.1093/mnras/stac439](https://doi.org/10.1093/mnras/stac439)

Zhang, W., Howell, L., Almgren, A., Burrows, A., & Bell, J. 2011, ApJS, 196, 20, doi: [10.1088/0067-0049/196/2/20](https://doi.org/10.1088/0067-0049/196/2/20)

Zou, L. 2021, arXiv e-prints, arXiv:2102.04435, doi: [10.48550/arXiv.2102.04435](https://doi.org/10.48550/arXiv.2102.04435)

## APPENDIX

## A. TWO RIEMANN PROBLEMS IN A SPHERICAL COORDINATE

In spherical coordinates, the Euler equations can be formulated using conservative variables based on linear momentum, following conventional numerical approaches. Alternatively, the  $\phi$ -momentum component can be replaced with angular momentum to improve conservation properties. The compact form of the linear momentum-based hydrodynamic equations (Equations 35–39) at the cell interfaces is expressed as follows:

$$\frac{\partial U_{\text{lm}}}{\partial t} + \frac{\partial F_{\text{lm}}}{\partial r} + \frac{\partial G_{\text{lm}}}{\partial \theta} = S_{\text{lm}}, \quad (\text{A1})$$

where,  $U_{\text{lm}}$ ,  $F_{\text{lm}}$ ,  $G_{\text{lm}}$ , and  $S_{\text{lm}}$  are the linear momentum based conserved quantities, fluxes, and source terms

$$U_{\text{lm}} = \begin{bmatrix} \rho \\ \rho v_r \\ \rho v_\theta \\ \rho v_\phi \\ E \end{bmatrix}, \quad F_{\text{lm}} = \begin{bmatrix} \rho v_r \\ \rho v_r^2 + p \\ \rho v_r v_\theta \\ \rho v_r v_\phi \\ v(E + p) \end{bmatrix}, \quad G_{\text{lm}} = \begin{bmatrix} \rho v_\theta \\ \rho v_r v_\theta \\ \rho v_\theta^2 + p \\ \rho v_\theta v_\phi \\ v(E + p) \end{bmatrix},$$

$$S_{\text{lm}} = \begin{bmatrix} 0 \\ \rho g_r + 2p/r + \rho(v_\phi^2 + v_\theta^2)/r \\ [\cot \theta(\rho v_\phi^2 + p) - \rho v_r v_\theta]/r \\ -(\rho v_r v_\theta - \cot \theta \rho v_\theta v_\phi)/r \\ \rho g_r v_r \end{bmatrix}. \quad (\text{A2})$$

Alternatively, the hydrodynamic equations written based on angular momentum read

$$\frac{\partial U_{\text{am}}}{\partial t} + \frac{\partial F_{\text{am}}}{\partial r} + \frac{\partial G_{\text{am}}}{\partial \theta} = S_{\text{am}}, \quad (\text{A3})$$

where

$$U_{\text{am}} = \begin{bmatrix} \rho \\ \rho v_r \\ \rho v_\theta \\ \rho l \\ E \end{bmatrix}, \quad F_{\text{am}} = \begin{bmatrix} \rho v_r \\ \rho v_r^2 + p \\ \rho v_r v_\theta \\ \rho v_r l \\ v(E + p) \end{bmatrix}, \quad G_{\text{am}} = \begin{bmatrix} \rho v_\theta \\ \rho v_r v_\theta \\ \rho v_\theta^2 + p \\ \rho v_\theta l \\ v(E + p) \end{bmatrix},$$

$$S_{\text{am}} = \begin{bmatrix} 0 \\ \rho g_r + 2p/r + \rho[(l/r \sin \theta)^2 + v_\theta^2]/r \\ \{\cot \theta[\rho(l/r \sin \theta)^2 + p] - \rho v_r v_\theta\}/r \\ 0 \\ \rho g_r v_r \end{bmatrix}. \quad (\text{A4})$$

While the left-hand side (LHS) of Equation A1 can be resolved using a standard Riemann solver (Toro 2013), Equation A3 presents a more complex solution structure. This is because the total energy,  $E$ , is coupled to the angular momentum in a non-trivial manner, as expressed by Equation 41. Numerical inconsistency arises when the Riemann solution from the linear-momentum-based Equation A1 is used to apply the flux divergence law to the angular-momentum-based state vector,  $U_{\text{am}}$ .

Ideally, one would solve the Riemann problem directly for Equation A3 and apply the flux divergence law to  $U_{\text{am}}$  to ensure the simultaneous and consistent conservation of both angular momentum and energy. However, given the significant analytical complexity of this approach, we instead propose the passive scalar angular momentum algorithm (PSAMA) in Section 3.1.2. This method prioritizes a more consistent angular momentum conservation formula to provide enhanced numerical robustness and stability, albeit at the cost of precise energy conservation—which is already subject to small deviations due to the iterative solvers used for radiation transport and gravitational source terms.

## B. DERIVATION OF PSAMA

After splitting the energy into two parts in Equation 41, we adapt Equation 39 correspondingly,

$$\frac{\partial E'}{\partial t} + \frac{1}{r^2} \frac{\partial [r^2(E' + p)v_r]}{\partial r} + \frac{1}{r \sin \theta} \frac{\partial [\sin \theta(E' + p)v_\theta]}{\partial \theta} + \frac{\partial e_{k\phi}}{\partial t} + \nabla \cdot (e_{k\phi} \vec{v}) = \rho g_r v_r. \quad (\text{B5})$$

The key is to express  $\partial e_{k\phi}/\partial t + \nabla \cdot (e_{k\phi} \vec{v})$  in terms of the known variables, the derivation is the following,

$$2 \frac{\partial e_{k\phi}}{\partial t} = \frac{\partial(\rho \Omega l)}{\partial t} = \Omega \frac{\partial \rho l}{\partial t} + \rho l \frac{\partial \Omega}{\partial t}, \quad (\text{B6})$$

where  $\Omega$  is the angular frequency around the  $z$  axis. Apparently, from Equation 40,

$$\Omega \frac{\partial \rho l}{\partial t} + \Omega \nabla \cdot (\rho \vec{v} l) = 0. \quad (\text{B7})$$

On the other hand, using continuity equation and Equation 40, we can obtain,

$$\rho \frac{\partial l}{\partial t} + \rho \vec{v} \cdot \nabla l = 0. \quad (\text{B8})$$

Substitute  $l = \Omega(r \sin \theta)^2$  and multiply by  $\Omega$ , the above equation becomes,

$$\rho l \frac{\partial \Omega}{\partial t} + \rho \Omega \vec{v} \cdot \nabla l = 0. \quad (\text{B9})$$

Adding Equation B7 and B9, we find,

$$2\frac{\partial e_{k\phi}}{\partial t} = -\Omega[\rho\vec{v} \cdot \nabla l + \nabla \cdot (\rho\vec{v}l)]. \quad (\text{B10})$$

Meanwhile,

$$\begin{aligned} \nabla l &= [(r \sin \theta)^2 \frac{\partial \Omega}{\partial r} + 2r(\sin \theta)^2 \Omega, \\ &\quad r(\sin \theta)^2 \frac{\partial \Omega}{\partial \theta} + 2r \sin \theta \cos \theta \Omega, 0]^T \\ &= (r \sin \theta)^2 \nabla \Omega + 2r \sin \theta \Omega [\sin \theta, \cos \theta, 0]^T \\ &= \frac{l}{\Omega} \nabla \Omega + 2\vec{v}_\Omega, \end{aligned} \quad (\text{B11})$$

where  $\vec{v}_\Omega = r \sin \theta \Omega [\sin \theta, \cos \theta, 0]^T$  is in principle similar to the origin of centrifugal force. Next, substitute Equation B11 into B10,

$$\begin{aligned} 2\frac{\partial e_{k\phi}}{\partial t} &= -\Omega \rho \vec{v} \cdot \left[ \frac{l}{\Omega} \nabla \Omega + 2\vec{v}_\Omega \right] - \Omega \nabla \cdot (\rho \vec{v}l) \\ &= -\nabla \cdot (\rho \vec{v} \Omega l) - 2\rho \Omega \vec{v}_\Omega \cdot \vec{v} \\ &= -\nabla \cdot (\rho \vec{v} \Omega l) - 2\rho \vec{f}_\Omega \cdot \vec{v}, \end{aligned} \quad (\text{B12})$$

where  $\vec{f}_\Omega = \Omega \vec{v}_\Omega = [v_\phi^2/r, v_\phi^2 \cot \theta/r, 0]$  is the centrifugal force. Therefore, reorganizing Equation B12, we obtain

$$\frac{\partial e_{k\phi}}{\partial t} + \nabla \cdot (e_{k\phi} \vec{v}) = -\rho \vec{f}_\Omega \cdot \vec{v}. \quad (\text{B13})$$

Not surprisingly,

$$\rho \vec{v} \cdot \vec{f}_\Omega = \rho \vec{v} \cdot \left[ \frac{v_\phi^2}{r}, \frac{v_\phi^2 \cot \theta}{r}, 0 \right]^T, \quad (\text{B14})$$

is the work done by the centrifugal force.

### C. SECOND ORDER INTEGRATION OF THE SOURCE TERMS

The Euler equations in a spherical coordinate will give rise to geometric source terms (see Equation 35-39), including  $2p/r$ ,  $\rho v_\phi^2/r$ ,  $p \cot \theta/r$ , etc. Each of them may become important in different regions, for example,  $2p/r$  or  $\rho v_\phi^2/r$  may balance the gravity in the radial direction in an atmosphere or an accretion disk, respectively. Mignone (2014) took a general approach to the source terms which may increase the complexity of the code. On the other hand, well-balanced scheme takes an assumed steady state solution into account (Käppeli 2022) that can cancel out most of the truncation error if the fluid is indeed close to the assumed steady state. In **Guangqi**, we hard code the source terms that are most relevant in astrophysics (geometric source terms and central gravity) and do not presume any steady state solutions. Because in many cases, we won't know which region is in which steady state.

The second order integration of the source term is done by making use of the slope limited hydrodynamic variables in a cell's volume integration. Specifically, the pressure source term in the spherical coordinate in  $\{i,j\}$  cell is

$$\int_V \frac{2p}{r} r^2 \sin \theta dr d\theta = \int_V 2pr \sin \theta dr d\theta, \quad (\text{C15})$$

where,

$$p = p_{i,j} + \frac{\partial p}{\partial r}(r - r_{i,j}) + \frac{\partial p}{\partial \theta}(\theta - \theta_{i,j}) \quad (\text{C16})$$

where,  $p_{i,j}$  is the average pressure of the cell,  $\frac{\partial p}{\partial r}$  and  $\frac{\partial p}{\partial \theta}$  are the slopes that are also used in the reconstruction step in Section 3.1.1, and  $r_{i,j}$  and  $\theta_{i,j}$  are the volume centric coordinate of the cell. When taking  $\partial p/\partial r = \partial p/\partial \theta = 0$ , the source term reduces to the first order case. The final expression of C15 is hard coded in **Guangqi**. In the same manner, we show how we calculate the gravitational work done to the gas in a spherical coordinate

$$\int_V \frac{\rho v_r}{r^2} r^2 \sin \theta dr d\theta = \int_V \rho v_r r^2 \sin \theta dr d\theta, \quad (\text{C17})$$

where,

$$\rho = \rho_{i,j} + \frac{\partial \rho}{\partial r}(r - r_{i,j}) + \frac{\partial \rho}{\partial \theta}(\theta - \theta_{i,j}), \quad (\text{C18})$$

$$v_r = v_{r,i,j} + \frac{\partial v_r}{\partial r}(r - r_{i,j}), \quad (\text{C19})$$

where we omit the  $\theta$  dependence in  $v_r$  for simplicity. The final expression also omit the product of the terms such as  $\partial \rho/\partial r \cdot \partial v_r/\partial r$  as they are high order terms.

By hard coding these source terms in **Guangqi**, we can maintain the hydrodynamic solver second order in space and time in the spherical coordinate without significantly increasing the computational cost. Section 5.3.2 has a steady state disk test that includes all the source terms and we show that the disk is maintained steady in **Guangqi** for thousands of orbits.